Utrecht University

Debye Institute

Nanophotonics Group

Phase imprinting of vortices in Bose-Einstein condensates using shaped light

Author:
Jasper Smits

Supervisor:
Prof. dr. P. van der Straten

July 8, 2016

Abstract

Vorticity in superfluids has been studied for decades. In atomic BECs, vorticity was induced by stirring with laser beams. In this thesis, phase imprinting is introduced as an alternative method to induce vorticity in a BEC. By using a Liquid Crystal-on-Silicon spatial light modulator the phase of a laser beam can be shaped into any spatial profile, limited only by the imaging resolution. By using this shaped light in a two-photon Raman transfer, the phase of the electromagnetic field is transferred on to the Bose-condensed atoms.

Simulations are performed for light containing a single phase winding, taking into account that the vortex in this beam has a finite vortex core size due to limited imaging resolution. It follows that the finite core size has an incomplete transfer as a result, but the phase winding is imprinted on to the atoms transferred to the second component.

Also, experimentally the two-photon Raman transition which is needed has been realised. However, the transfer process is impeded by a different two-photon process occuring at the same time, and by superradiant Rayleigh scattering. Recommendations are given to suppress these effects and successfully imprint the phase from the shaped light on to the atoms.

Contents

1 Introduction

Since the discovery of superfluidity in Helium-4 by Pyotr Kapitsa and John F. Allen in 1937 [1,2], superfluids have been a target of research. The most well known characteristic of a superfluid is frictionless flow, the ability to flow around an obstacle unimpeded and without the production of heat. Another, less well known property, is the presence of quantized vortices. Superfluids, due to their quantummechanical nature, do not allow the existence of arbitrarily sized vortices. Instead, vorticity in superfluids is exhibited in terms of vortex lines, each carrying a single quantum of rotation.

In 1995, the first atomic Bose-Einstein condensate (BEC) was realised by Eric Cornell and Carl Wieman [3]. Atomic BECs exhibit superfluidic properties just like Helium-4. However, the interaction between particles in atomic gases is a lot smaller than in Helium-4 and the system is very well isolated from its surroundings. This allows for experiments on the Bose-Einstein condensate in a completely controlled environment. The vortex experiments known from Helium-4 were reproduced in atomic gases and produced beautiful lattices of vortices, so-called Abrikosov lattices [4]. Lattices in these experiments are made by stirring the atomic cloud using a laser beam.

However, with atomic gases there are more possibilities. Since the system is very well isolated from its surroundings and all atoms occupy the same quantum-mechanical state, one can use the electronic structure of the individual atoms in the condensate. One can manipulate the magnetic fields used to trap the atoms to induce a Berry phase. Or, by coupling two ground states together using a two-photon transition, a physicist is able to set this superfluid in motion by manipulating the laser beams used to couple these states. A whole number of excitations, including vortices, can be created in the process.

Using a two-photon process is a more controlled way of inducing excitations, compared to stirring or manipulating the fields. Instead of appealing to its hydrodynamic properties, for example through stirring, this new technique uses the quantummechanical properties of the condensate to induce excitations.

This thesis will work towards using a two-photon coupling between two ground states to induce vorticity in a Bose-Einstein condensate. Firstly, theory is developed to describe the coupling of the two ground states. Secondly, the spatial light modulator (SLM) used to manipulate the light is discussed and a test setup is build to demonstrate its effectiveness. Based on results from the tests with the spatial light modulator, a simulation of the transfer process of the atoms is performed. Finally, to perform the experiment a setup is built and tested.

2 Experimental Setup

Making Bose-Einstein condensates requires extreme conditions. Very low background pressures, up to 10^{-12} mbar, have to be achieved in order to cool atoms to the condensation temperature. In Utrecht we condense sodium atoms to this temperature using a combination of laser cooling and evaporative cooling. This section will discuss the properties of sodium, the laser and vacuum systems and cooling mechanisms.

2.1 Properties of sodium

Sodium is an alkali metal with a single stable, bosonic isotope, sodium-23. Since alkali atoms only have one electron in the outer shell, the electronic structure of alkali atoms is relatively simple. This allows laser cooling on the so-called "D-lines". Our laser cooling takes place on the $3^2S_{1/2}$, $F = 2$ to $3^2P_{3/2}$, $F' = 3$ transition. The properties of sodium and the cycling transition can be found in table 1. The level scheme for the D_2 line is given further on, in figure 2.1.

Table 1: Basic properties of sodium-23, as well as the scattering lengths of the relevant atom species in the $F = 1$ ground state manifold.

Basic properties	
Atomic mass m	22.990 u [5]
	3.817×10^{-26} kg
Melting point T_{M}	97.81 °C [6]
	370.95 K
Scattering lengths	
$a_{-1,-1}$	$52.98\, a_0$ [7]
	2.804 nm
$a_{0,-1}$	$52.98\, a_0$ [7]
	2.804 nm
$a_{0,0}$	$51.10\, a_0$ [7]
	2.704 nm
Cycling transition properties [8]	
Vacuum wavelength λ_0	589.15220(15) nm
Frequency ω_0	$2\pi \times 508.8487162(13)$ THz
Linewidth Γ	$2\pi \times 9.746(46)$ MHz
Lifetime τ	16.2492(77) ns
Recoil velocity v_{r}	2.9461 cm/s
Doppler Temperature T_{D}	235.03 μK
Saturation intensity I_{s}	6.2600(21) mW/cm^2

2.2 Laser system

To generate the light used to cool, manipulate and image the atoms in our setup, two laser systems[1] are used. The cooling laser is locked to the $F = 2$ to $F' = 3$ transition and is used to create the MOT beams and Zeeman slower beam. Light from this laser is also used to perform the Raman transition in the experiment. The repump laser is locked to the $F = 1$ to $F' = 1, 2$ crossover. Light from this laser is used to do repumping, (resonant) probing and polarization of the atoms. A complete image of the setup can be found in figure 2.2. There is also the possibility of locking one laser to the other. This system is currently being developed in-house.

[1] Toptica TA-SHG Pro

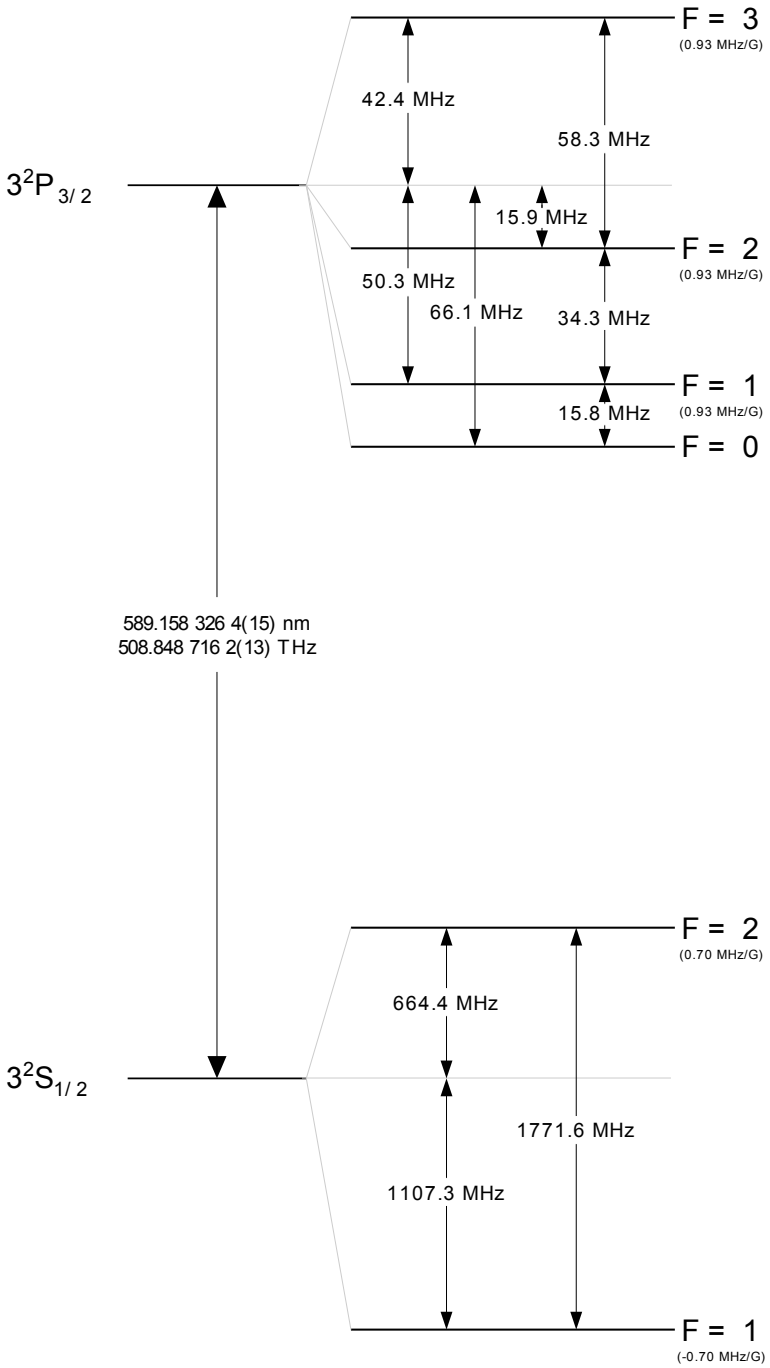

Figure 2.1: The level scheme for the D_2 transition in sodium-23. Lines on the right are the different cooling and repump lasers used in the final experiment. Values for the level splittings taken from [8].

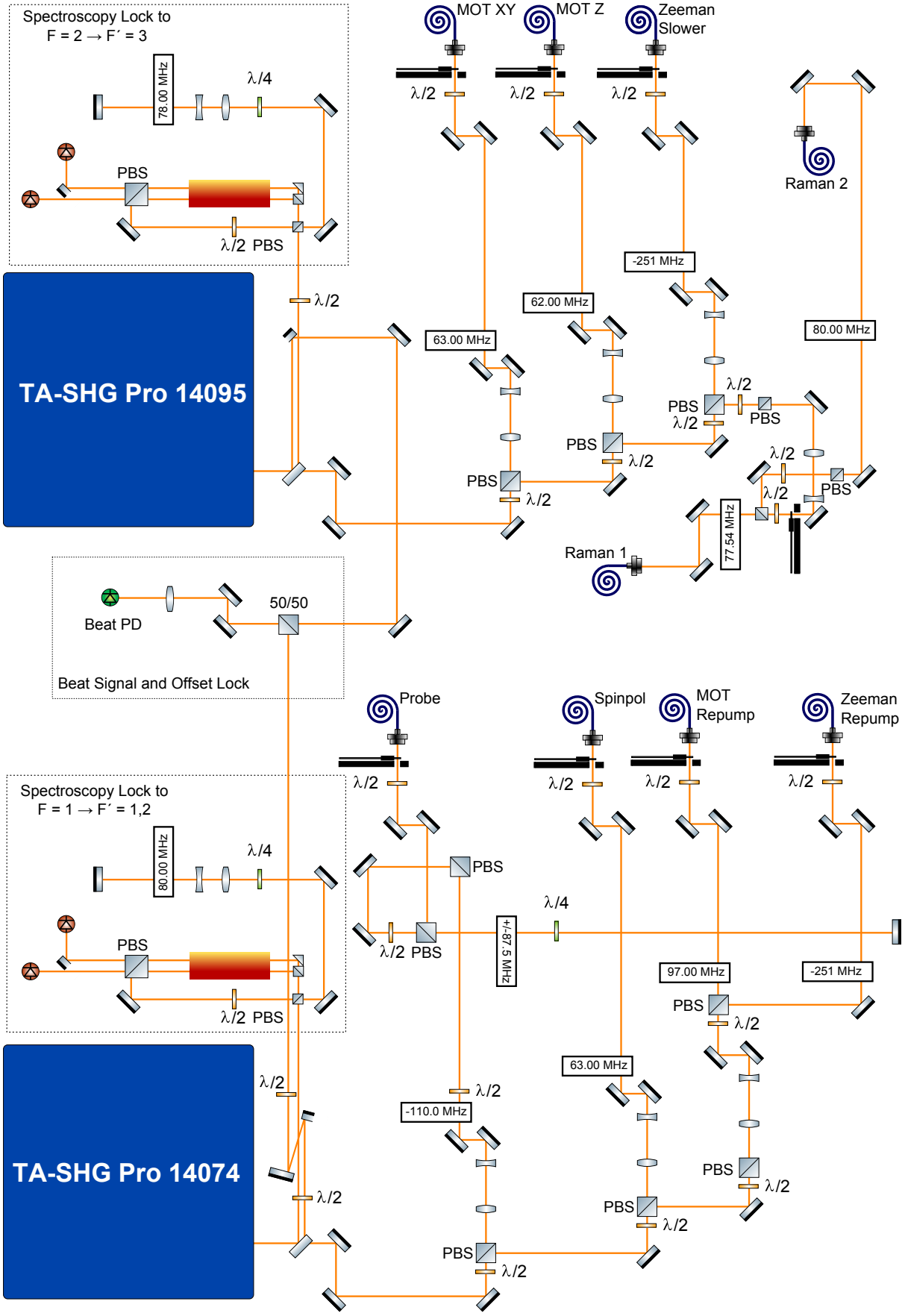

Figure 2.2: Layout of the laser table on which the two cooling lasers are located.

2.3 Vacuum layout

To achieve Bose-Einstein condensation, extremely high vacuum ($\sim 10^{-11}$ mbar) is needed. This subsection will briefly discuss the layout of the vacuum chambers in the experiment. The vacuum setup is divided into three compartments: the oven, zeeman slower, and experimental chamber. Between compartments,electronically operated pneumatic valves are installed. While not in operation, these valves are closed to make sure any problem with the vacuum in one of the compartments does not influence the others. In addition, between all the high-vacuum pumps and roughing pumps, electronically operated pneumatic valves are also present.

2.3.1 Oven

A small amount of sodium is heated to $\sim 300\,^{\circ}$C in an oven. The pressure in the oven section is approximately 1.3×10^{-7} mbar while turned off and approximately 3×10^{-7} mbar while in operation. Pressure is maintained by a pair of pumps consisting of an oil diffusion pump and a dual-stage rotary vane pump[2]. The atom gas is shaped by 2 diaphragms into a jet while exiting the oven, due to its vapor pressure. The tertiary chamber of the oven contains a cold plate, which can be cooled with liquid nitrogen to further decrease the pressure in the oven. This prevents contaminants from the oven from reaching the Zeeman slower and experimental chamber.

2.3.2 Zeeman slower

The Zeeman slower consists of two stages. A 1.8 meter-long section and a small secondary section right before the experimental chamber, for additional slowing. Pressures in the Zeeman slower, while idle, are $< 5.0 \times 10^{-9}$ mbar near the oven and 9.5×10^{-10} mbar near the experimental chamber. During operation these pressures increase to 1.0×10^{-8} mbar and $1.2 - 1.5 \times 10^{-9}$ mbar respectively. The Zeeman slower is pumped at both ends by turbomolecular pumps. The pump nearest to the experimental chamber has a drag pump attached to decrease the pressure at the pump exhaust for increased pumping power. This drag pump and the other turbo pump have their exhausts connected to a common roughing pump[3]. The pressure in the intermediate section between the high-vacuum pumps and roughing pump is approximately 1.3×10^{-4} mbar.

2.3.3 Experimental chamber

The Zeeman slower and experimental chamber are connected by a long, thin tube, functioning as differential pump section. The experimental chamber is pumped by two pumps: an ion pump and a titanium sublimation pump. To further decrease the pressure while in operation, part of the experimental chamber is cooled using liquid nitrogen. The low temperature causes additional atoms to be trapped, further reducing the pressure. While the setup is not in use, the cold plate thaws and the additional atoms are pumped away. Using these pumps, a final pressure of $\sim 5 \times 10^{-12}$ mbar can be reached in the experimental chamber.

2.3.4 Fail-safe system

While the Zeeman slower and oven can endure atmospheric pressures for short time, a high pressure in the experimental chamber can result in catastrophic failure of the ion pump and, due to saturation of the chamber walls with particles, may result in weeks of pumping. If, at any point, one of the pumps should fail, a fail-safe system[4] will close the valves associated with the compromised compartment. In addition, if the back pressure of the high-vacuum pumps is too high, these will automatically shut off. This is to prevent further damage to the pumps and to make sure problems with the vacuum remain isolated to each compartment.

[2] Edwards RV12
[3] Edwards E2M40
[4] Designed in-house

2.4 Laser cooling

As mentioned in the previous subsection, the source of atoms is the oven heated to approximately 600 K. The atom jet, shaped by 2 diaphragms, enters the Zeeman slower at approximately 800 m/s. In this subsection, the laser cooling process is briefly described.

2.4.1 Zeeman slower

In the Zeeman slower a combination of two overlapped laser beams, a laser at ~ 130 mW sourced from the cooling laser and a repump lasers at ~ 15 mW sourced from the repump laser, decelerate the atoms. The atoms cycle on the $(F, m_F) = (2, 2) \rightarrow (F', m_{F'}) = (3, 3)$ transition. The Zeeman slower has a zero crossing, prompting the need for a repump laser. The repump laser also compensates for atoms leaving the $F = 2$ manifold due to a number of other reasons. After the main Zeeman slower, which is a 1.8 meter long solenoid-like magnet, atoms enter an intermediate vacuum chamber. After this, a small section provides additional slowing. Atoms enter the experimental chamber at approximately 70 m/s.

2.4.2 Magneto-optical trap

The magneto-optical trap (MOT) consists of a repump laser and a number of trapping lasers locked to the cycling transition. The magnetic field for the MOT is generated by two coils in anti-Helmholtz configuration. The trapping lasers come from two different fibers. For the short direction, along the cylindrical axis of the trapping coils, a laser beam with a diameter of approximately 18 mm is used and reflected to provide a second beam of the same intensity. For the other two directions, a laser beam with a diameter of approximately 40 mm is split into two equal components. These, passing through the vacuum chamber, make a 45° angle with gravity. Both these beams are reflected to provide the counter-propagating component. The two cooling lasers are detuned 1 MHz with respect to each other to prevent the formation of a static lattice. The repump beam is incident at an angle of roughly 45° with respect to gravity as well. This beam contains a 'dark spot', allowing atoms in the center of the trap to leave the cycling transition, reducing radiation pressure in the center, allowing much higher atom densities in the MOT. The temperature of the MOT is determined by release/recapture measurements (appendix A) and is approximately 500 μK. This is relatively high compared to the Doppler temperature $T_{\mathrm{D}} = 235\,\mu$K. The high temperature of the MOT can be narrowed down to a problem in the 'short' direction of the trap. However, to date the problem has not een pinpointed exactly and thus has not been resolved.

2.5 Magnetic trapping

After trapping the atoms in the MOT, atoms are transferred to the magnetic trap (MT). The magnetic trap consists of a cloverleaf trap to provide radial confinement and two pairs of coils, the 'pinch' and 'bias' coils, in Helmholtz configuration to provide axial confinement. Since only atoms in the $(F, m_F) = (1, -1)$ state can be trapped, the atoms are spin-polarized in a high magnetic field. This transfers a large fraction of the atoms to the trapped state, allowing transfer efficiencies of up to 65%, compared to the 33% theoretical value when no spin polarization is used. During the transfer, the Helmholtz coils used for axial confinement carry unequal current. This causes the center of the trap to be at ~ 100 G and also improves mode-matching between the MOT and the MT. During the loading process, the current running through the pinch and bias coils is ramped to be equal, while the current through the cloverleaf trap is also increased. This compresses the trap further.

2.6 Evaporative cooling

Once atoms are transferred to the magnetic trap, evaporative cooling is used to cool down the sample even further. To perform evaporative cooling, an RF field is slowly ramped down. Atoms which carry the most energy are able to reach regions with higher magnetic fields. Due to the Zeeman shift the RF field will transfer these atoms from the $m_F = -1$ substate to the other substates, removing them from the trap. Since atoms with higher-than-average energy are removed, the total temperature of the sample goes down. Bose-Einstein condensation is reached after 80 seconds, with approximately 10^7 atoms in a

$(\omega_x, \omega_y, \omega_z) = 2\pi \times (14.6, 14.6, 104)$ Hz harmonic trap. A detailed description of the evaporative cooling, as well as a simulation of the evaporative cooling process can be found in [9].

2.7 Imaging the atom cloud

To probe the atoms, two imaging techniques are available. The traditional absorption imaging, in which atoms are allowed to expand before taking an image to lower the optical density, and phase contrast imaging, which is an imaging technique suitable for the high densities which present themselves when imaging atoms in-situ. In the experiment, absorption imaging is used in conjunction with Stern-Gerlach splitting. Stern-Gerlach splitting allows separation of different spin components, such that these can be studied independently.

2.8 Experimental control

The experiment is controlled from a computer running WordGenerator, which sends the experimental sequence to the National Instruments cards connecting to the experiment. This setup allows control of up-to 32 digital channels and 8 analog channels. Through a serial controller, the DDS generating the frequencies for the RF-cooling is controlled. Of the analog channels, five are reserved for control of the magnetic coils. Every AOM and shutter in figure 2.2 also has its respective digital channel.

3 Theory

The experiment in this thesis relies heavily on coupling two spin components of the BEC using Raman coupling. In this section, a coupled Gross-Pitaevskii equation (GPE) is derived which describes the dynamics of the BEC at $T = 0$ during and after Raman coupling two components. The equations are derived through Euler-Lagrange equations of motion from appropriately formulated action. First, a single component GPE is derived. Consequently, the action is given for two components and equations of motion are obtained. Finally, Raman coupling is added and the entire expression is combined into a single action, from which the equations of motion for the full problem are determined.

3.1 One-component BEC

For a single component BEC, the GPE can be derived from the action

$$S_1[\psi] = \int \mathrm{d}^3x\, \mathrm{d}t\, \psi^*(\mathbf{r},t) \left[i\hbar\frac{\partial}{\partial t} + \frac{\hbar^2}{2m}\nabla^2 - U(\mathbf{r}) - \frac{1}{2}gN|\psi(\mathbf{r})|^2 + \mu \right] \psi(\mathbf{r},t). \tag{3.1}$$

The first term in the brackets takes the time-dependence into account. The second to fourth terms lead to the energy functional of the GPE, respectively the momentum, the potential and the interaction parts. The last term, μ, is the chemical potential. This is the energy needed to add a single particle to the system. The wavefunction ψ is normalized to unity, hence the non-linear interaction term is multiplied by the particle number N. The non-linear coupling strength g is given by $g = \frac{4\pi\hbar^2 a_s}{m}$, where a_s is the s-wave scattering length. The Gross-Pitaevskii equation follows by calculating the Euler-Lagrange equations with respect to ψ^*,

$$\frac{\delta S}{\delta \psi^*} = 0.$$

Doing this yields

$$i\hbar\frac{\partial}{\partial t}\psi(\mathbf{r},t) = \left[-\frac{\hbar^2}{2m}\nabla^2 + U(\mathbf{r}) + gN|\psi(\mathbf{r},t)|^2 - \mu \right] \psi(\mathbf{r},t). \tag{3.2}$$

This is the one-component Gross-Pitaevskii equation, or non-linear Schrödinger equation as known in literature [10].

3.2 Two-component BEC

For the experiment, a coupled, two-component Gross-Pitaevskii equation is needed. Using the action from Eq. (3.1), it is possible to generalize to multiple components and to add couplings between these components. The different components also have a non-zero intercomponent scattering interaction. Combining both in one action yields

$$S_2[\psi_1,\psi_2] = \int \mathrm{d}^3x\, \mathrm{d}t \sum_{i=1,2} \psi_i^*(\mathbf{r}) \left[i\hbar\frac{\partial}{\partial t} + \frac{\hbar^2}{2m}\nabla^2 - U_i(\mathbf{r}) - \frac{1}{2}\sum_{j=1,2} g_{ij}N|\psi_j(\mathbf{r})|^2 + \mu \right] \psi_i(\mathbf{r}). \tag{3.3}$$

Normalization of the wavefunctions $\psi_{1,2}$ is chosen such that

$$\int \mathrm{d}^3x \left(|\psi_1(\mathbf{r})|^2 + |\psi_2(\mathbf{r})|^2 \right) = 1.$$

The potential $U_i(\mathbf{r})$ can differ for each component i, since different spin states might experience a different potential from the same magnetic field. Similar to the one-component case, the equations of motion are derived using the Euler-Lagrange equation. The result is

$$\frac{\delta S_2}{\delta \psi_1^*} = 0 \quad \Longrightarrow \quad i\hbar\frac{\partial}{\partial t}\psi_1(\mathbf{r},t) = \left[-\frac{\hbar^2}{2m}\nabla^2 + U_1(\mathbf{r}) + g_{11}N|\psi_1(\mathbf{r},t)|^2 + g_{12}N|\psi_2(\mathbf{r},t)|^2 - \mu \right] \psi_1(\mathbf{r},t), \tag{3.4a}$$

$$\frac{\delta S_2}{\delta \psi_2^*} = 0 \quad \Longrightarrow \quad i\hbar\frac{\partial}{\partial t}\psi_2(\mathbf{r},t) = \left[-\frac{\hbar^2}{2m}\nabla^2 + U_2(\mathbf{r}) + g_{12}N|\psi_1(\mathbf{r},t)|^2 + g_{22}N|\psi_2(\mathbf{r},t)|^2 - \mu \right] \psi_2(\mathbf{r},t). \tag{3.4b}$$

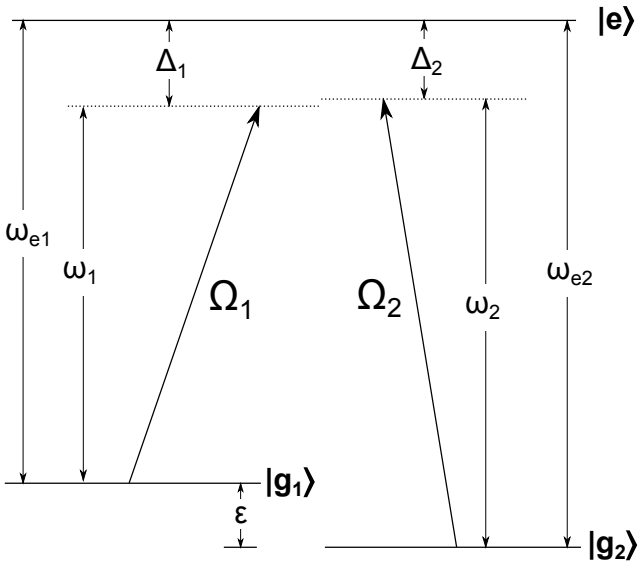

Figure 3.1: Schematic representation of a Λ three-level system. The transitions are driven by electromagnetic fields with frequencies ω_1 and ω_2 with corresponding Rabi frequencies Ω_1 and Ω_2. The resonance frequency or level splitting, in both cases, is given by ω_{ei} for $i = 1, 2$ and results in a detuning $\Delta_i = \omega_i - \omega_{ei}$. The level splitting of the ground states is given by $\epsilon = \omega_{e2} - \omega_{e1}$.

3.3 Raman coupling

In the experiment the two components of the BEC are coherently coupled through a two-photon Raman process. In this subsection we will briefly discuss three-level systems. We will work with a Λ three-level system, a schematic representation of which can be seen in figure 3.1. A detailed discussion of such as system can be found in Ref. [11, Ch. 23]. An isolated atom is discussed here. The optical frequencies are chosen such that detunings $\Delta_1 = \Delta_2 \equiv \Delta$. This yields, for the Hamiltonian of the system, in the rotating wave approximation, the following expression

$$\mathcal{H} = \frac{\hbar}{2}\begin{pmatrix} 0 & \Omega_1^* & 0 \\ \Omega_1 & 2\Delta & \Omega_2 \\ 0 & \Omega_2^* & 0 \end{pmatrix} \qquad \text{on spinor} \qquad \Psi' = \begin{pmatrix} \psi_{\mathrm{g}_1} \\ \psi_{\mathrm{e}} \\ \psi_{\mathrm{g}_2} \end{pmatrix}. \tag{3.5}$$

This result can be further simplified. If the detuning Δ is sufficiently large compared to the Rabi frequencies Ω_1 and Ω_2, *i.e.* $\Delta \gg \Omega_1, \Omega_2$ then the excited state ψ_e can be eliminated since population in this level will be neglible. This is done by assuming that $\partial_t \psi_{\mathrm{e}} = 0$, which yields

$$\psi_e = -\frac{\Omega_1}{\Delta}\psi_{\mathrm{g}_1} - \frac{\Omega_2}{\Delta}\psi_{\mathrm{g}_2}. \tag{3.6}$$

The Hamiltonian will change to

$$\mathcal{H} = \frac{\hbar}{2}\begin{pmatrix} \frac{|\Omega_1|^2}{\Delta} & \Omega_{\mathrm{eff}} \\ \Omega_{\mathrm{eff}}^* & \frac{|\Omega_2|^2}{\Delta} \end{pmatrix} \qquad \text{on spinor} \qquad \Psi = \begin{pmatrix} \psi_{\mathrm{g}_1} \\ \psi_{\mathrm{g}_2} \end{pmatrix}, \tag{3.7}$$

where

$$\Omega_{\mathrm{eff}} = \frac{\Omega_1^* \Omega_2}{\Delta},$$

is the effective Rabi frequency. This result is a diagonal shift in the energy levels, known as the light shift, and an off-diagonal coupling between the components. The Hamiltonian can be converted to a contribution to the action of Eq. 3.3. The corresponding contribution is given by

$$S'[\Psi] = -\frac{\hbar}{2}\int \mathrm{d}^3x\,\mathrm{d}t\,\begin{pmatrix} \psi_1^* & \psi_2^* \end{pmatrix}\begin{pmatrix} \frac{|\Omega_1|^2}{\Delta} & \Omega_{\mathrm{eff}} \\ \Omega_{\mathrm{eff}}^* & \frac{|\Omega_2|^2}{\Delta} \end{pmatrix}\begin{pmatrix} \psi_1 \\ \psi_2 \end{pmatrix}. \tag{3.8}$$

This result can be merged into the action of section 3.2.

3.4 Coupled GPE

Using results from the previous two subsections, a Raman coupled GPE for a two-component spinor BEC is formulated. This results in

$$S_{\text{coup}}[\psi_1,\psi_2] = \int \mathrm{d}^3x\,\mathrm{d}t\,\left\{-\frac{\hbar}{2}\begin{pmatrix}\psi_1^* & \psi_2^*\end{pmatrix}\begin{pmatrix}\frac{|\Omega_1|^2}{\Delta} & \Omega_{\text{eff}} \\ \Omega_{\text{eff}}^* & \frac{|\Omega_2|^2}{\Delta}\end{pmatrix}\begin{pmatrix}\psi_1 \\ \psi_2\end{pmatrix}\right.$$
$$\left. + \sum_{i=1,2}\psi_i^*(\mathbf{r})\left[i\hbar\frac{\partial}{\partial t} + \frac{\hbar^2}{2m}\nabla^2 - U_i(\mathbf{r}) - \frac{1}{2}\sum_{j=1,2} g_{ij}N|\psi_j(\mathbf{r})|^2 + \mu\right]\psi_i(\mathbf{r})\right\}. \quad (3.9)$$

Deriving the Euler-Lagrange equations of motion with respect to ψ_1^* and ψ_2^* yields the Raman-coupled GPE. The equations of motion are written in matrix form

$$i\hbar\frac{\partial}{\partial t}\begin{pmatrix}\psi_1 \\ \psi_2\end{pmatrix} = \begin{pmatrix}\mathcal{H}_1 & \frac{\hbar\Omega_{\text{eff}}}{2} \\ \frac{\hbar\Omega_{\text{eff}}^*}{2} & \mathcal{H}_2\end{pmatrix}\begin{pmatrix}\psi_1 \\ \psi_2\end{pmatrix}, \quad (3.10)$$

where

$$\mathcal{H}_i = -\frac{\hbar^2}{2m}\nabla^2 + U_i(\mathbf{r}) + \sum_{j=1,2} g_{ij}N|\psi_j(\mathbf{r})|^2 + \frac{\hbar|\Omega_i|^2}{2\Delta} - \mu.$$

It is seen that the coupling is a result of the off-diagonal terms in the Hamitonian matrix. It is also determined that, aside from the light shift, the diagonal elements are not modified. This implies that the dynamics of the BEC do not change. However, the two components are coupled through the electromagnetic fields by an effective Raman coupling. Equation (3.10) provides an equation of motion which fully describes the system studied in the experiment at zero temperature.

3.4.1 Validity of approximations

In subsection 3.3 it is assumed that the two detunings $\Delta_{1,2}$ of figure 3.1 are equal. However, from the equations of motion of Eq. (3.10) it follows that the level spacing between these two energy states might vary spatially, as is the case if the potentials U_i are not the same for $i = 1, 2$. In the experiment the level spacing between the two components follows from the fact that the second component does not interact with the magnetic field at all, while the first component experiences harmonic trapping. Thus $U_2 = 0$, while $U_1 \propto \mathbf{r}^2$. Ignoring the Raman coupling, the level spacing difference over the entire atom cloud of the first component can be estimated. Using the Thomas-Fermi approximation it is estimated that the splitting over the entire cloud can vary at most $\mu/h \sim 2\,\text{kHz}$. When compared to the single-photon linewidth of the Raman process, which is typically 50 kHz, this effect can be safely ignored.

3.5 Phase imprinting

To model phase imprinting, the Rabi frequencies are related to the electric field. The electric field of the used light can be described by

$$\vec{\mathcal{E}} = \hat{\varepsilon}\mathcal{E}_0 \cos[kz - \omega t - \varphi(x, y)], \tag{3.11}$$

where $\varphi(x, y)$ indicates the induced phase delay, with negative sign for convenience later, and the remaining terms within the brackets describe a plane wave propagating along the z-direction. The electric field amplitude $\mathcal{E}_0$ is a real quantity and $\hat{\varepsilon}$ indicates the polarization vector. From the electric field the Rabi frequencies can be determined. For a detailed calculation of the Rabi frequencies and all involved approximations, consult Ref. [11, Ch. 2 & 3]. Taking into account the induced phase factor from Eq. (3.11), the Rabi frequency is given by

$$\Omega = -\frac{\mathcal{E}_0 \hat{\varepsilon} \cdot \vec{\mu}}{\hbar} e^{i\varphi(x,y)}, \tag{3.12}$$

where $\vec{\mu}$ is the dipole moment associated with the transition. From the oscillating electric field in Eq. (3.11) only one of the complex exponents (of the cosine) is taken into account, due to the rotating wave approximation. While the electric field is a real quantity, the Rabi frequency can be complex. For clarity, the Rabi frequencies are denoted as

$$\Omega_i = \Omega_0 e^{i\varphi_i(x,y)},$$

where Ω_0 is a real quantity, common to both Rabi fields. All phase information is thus stored in the parameter $\varphi(x, y)$.

For phase imprinting, the first Rabi field is chosen to have a phase profile $\varphi(x, y)$ while the second Rabi field is a plane wave, thus

$$\Omega_1 = \Omega_0 e^{i\varphi(x,y)} \qquad \text{and} \qquad \Omega_2 = \Omega_0.$$

Using these values in the action of Eq. (3.8), the result is

$$S'[\Psi] = -\frac{\hbar}{2} \int \mathrm{d}^3x \, \mathrm{d}t \begin{pmatrix} \psi_1^* & \psi_2^* \end{pmatrix} \begin{pmatrix} \Omega_{\text{eff}} & \Omega_{\text{eff}} e^{i\varphi(x,y)} \\ \Omega_{\text{eff}} e^{-i\varphi(x,y)} & \Omega_{\text{eff}} \end{pmatrix} \begin{pmatrix} \psi_1 \\ \psi_2 \end{pmatrix}. \tag{3.13}$$

where $\Omega_{\text{eff}} = \Omega_0^2/\Delta$, a real quantity. By setting $\tilde{\psi}_2(x, y) = \psi_2(x, y)e^{i\varphi(x,y)}$, the equation (3.13) can be rewritten to

$$S'[\Psi] = -\frac{\hbar}{2} \int \mathrm{d}^3x \, \mathrm{d}t \begin{pmatrix} \psi_1^* & \tilde{\psi}_2^* \end{pmatrix} \begin{pmatrix} \Omega_{\text{eff}} & \Omega_{\text{eff}} \\ \Omega_{\text{eff}} & \Omega_{\text{eff}} \end{pmatrix} \begin{pmatrix} \psi_1 \\ \tilde{\psi}_2 \end{pmatrix}. \tag{3.14}$$

This does not change the value of the action, but the wavefunction $\tilde{\psi}$ now contains the phase profile. Adding the phase profile in the electromagnetic field can be interpreted as changing the bare states of the coupling from ψ_1 and ψ_2 to ψ_1 and $\psi_2 e^{i\varphi(x,y)}$. The shaped wave couples the first component to the second component, but with a phase profile included in the second component. This is the principle on which phase imprinting relies.

4 Spatial Light Modulator

In section 3, it has been discussed how to perform phase imprinting. This section will discuss the spatial light modulator used to generate light beams containing the phase profile which will be imprinted on to the atoms. For the experiment, a phase-only SLM[5] was chosen. The SLM is used in reflection and allows modulation of phase at each pixel through in-plane rotation of birefringent liquid crystals suspended near a CMOS substrate. Rotation of these crystals will alter the optical path length at each pixel, allowing any phase pattern to be created at the SLM. To keep the liquid crystals aligned, the SLM refreshes the voltage at each pixel periodically. An overview of the relevant SLM specifications is given in table 2.

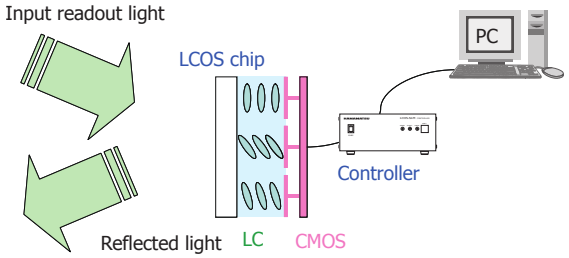

Figure 4.1: General working principle of the used SLM. Image taken from Hamamatsu Technical Specifications sheet for X10468-series SLM.

Table 2: Specifications of the SLM employed in the experiment. Data from Ref. [12].

Utilization wavelength	$650 \pm 50\,\mathrm{nm}$
Light utilization	95%
Pixels	792×600
Pixel Pitch	$20\,\mu\mathrm{m}$
Signal levels	256
Refresh frequency	$120\,\mathrm{Hz}$

4.1 Test setup

Before employing the SLM in the setup, it was tested in a seperate test setup. As a test setup a Michelson interferometer was used. The SLM replaces one of the two mirrors. A schematic representation of the test setup is shown in figure 4.2.

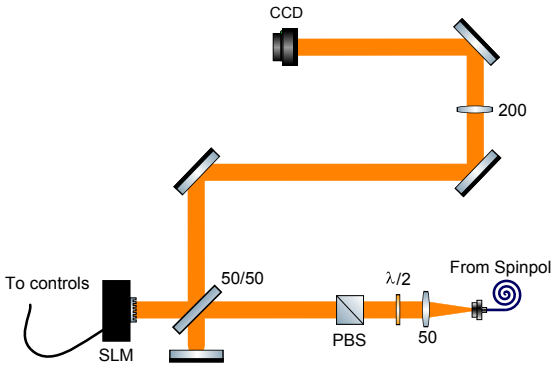

Figure 4.2: Schematic representation of the setup used to test the SLM. Light is supplied by the repump laser through the spin polarization beam path.

Using this setup the SLM is imaged on the camera. It is possible to study interference, or, by blocking the reference beam, it is also possible to study intensity fluctuations which are a result of the phase

[5] Hamamatsu LCOS, X10468-06

modulation or imperfect imaging of the SLM. By considering both intensity and interference with the reference, it is possible to resolve the electromagnetic field amplitude and phase up to a global phase factor.

To demonstrate the setup, the *International Year of Light 2015*-logo was converted to black-and-white and displayed on the SLM. The beam from the SLM is made to interfere with the reference beam. Through this experiment, the phase imprinting technique can be tested before it is implemented as shaped light in the setup. The conversion to black-and-white is done such that the logo is modulated exactly π compared to the background. This results in an interference pattern in which the logo is clearly visible. The results of this test can be seen in figure 4.3, where (a-d) represent the original logo (a), the black-and-white version for display on the SLM (b), the image on the camera as a result of this pattern (c), and the interference pattern without the logo displayed on the SLM (d). From this test, it is shown that a spatially varying phase pattern can be imaged just as one would image a regular image.

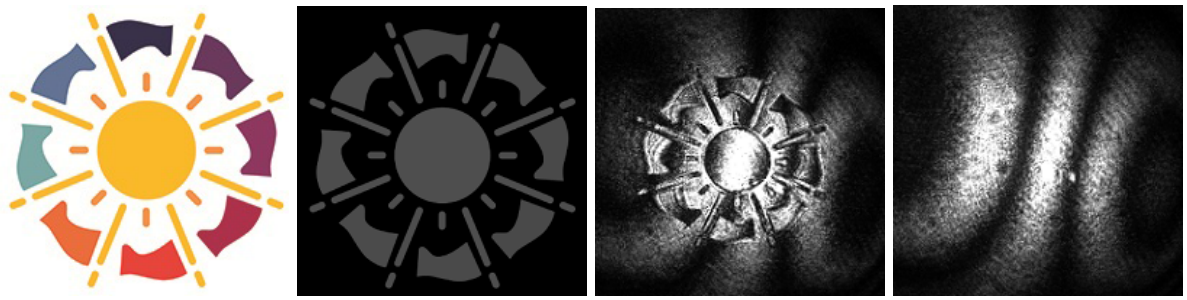

(a) **(b)** **(c)** **(d)**

Figure 4.3: **(a)** International year of light logo **(b)** Conversion to black-and-white to display on the SLM **(c)** Interference of the phase of the logo with the reference beam **(d)** No pattern on SLM.

4.2 Vortices

Among phase defects studied in BEC, vortices are the most prominent. Generating vortices has previously been done through stirring with laser beams and subsequently waiting for the system to equilibrate, which, depending on the stirring frequency, would generate an Abrikosov lattice of singly charged, same-sign vortices. The phase imprinting technique suggested here allows any phase pattern, no matter how complex, where the only limit is the resolution of the imaging setup. A single optical vortex can easily be generated by displaying a 0 to 2π phase winding on the SLM. This can be expanded to generate vortices with arbitrary charge number. A test measurement in which such optical vortices where created can be seen in figure 4.4. From (b) and (c) it can be seen that the vortices have a finite core size depending on their charge and the resolution of the projection optics. From preliminary measurements in the test setup, a vortex core size of approximately 20 μm was determined. The fringing in (b) and (c) is a result of interference with an non-diffracted portion of the light with the grating pattern.

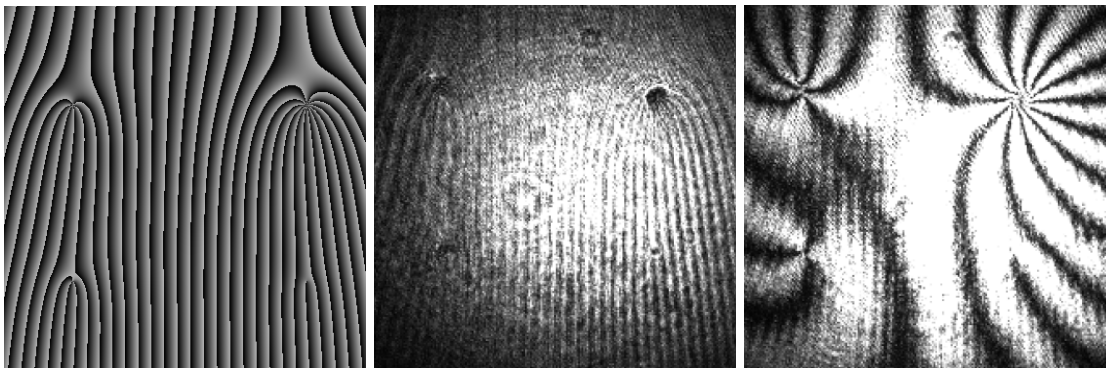

(a) **(b)** **(c)**

Figure 4.4: **(a)** Phase pattern displayed on the SLM to generate vortices with charge 1, 3, 6 and 12. Also visible is a grating, to seperate the non-diffracted light from the diffracted light. In addition, a small curvature is given to the pattern to compensate for the curvature of the chip. **(b)** Intensity pattern seen in the test setup when the pattern from (a) is displayed on the SLM. **(c)** Interference pattern due to interference with the reference beam, seen in the test setup when the pattern from (a) is displayed on the SLM.

5 Simulations

In section 4 it is shown that, due to finite resolution of the projection optics, the mapping of the SLM on to the atoms will have a finite resolution. To determine the effect of a finite resolution on the phase imprinting process, a simulation is run of the atom transfer. Since the effects under study exhibit themselves at length scales of the healing length, a simulation which can resolve the healing length will be needed. To save computation time, the GPE from section 3 will be reduced to 2D.

5.1 Numerical algorithms

To perform time-evolution on the system, the time-dependent GPE is used. The time-dependent GPE can be divided into two parts. One part depending on the position x in the grid, while the other part depends on the momentum $\hat{k} = i\nabla$. The equation is split according to its dependence to either position or momentum, *i.e.*:

$$i\partial_t\psi = \{L_1(\hat{x}) + L_2(\hat{k})\}\psi.$$

The wavefunction can also be expressed in the k-basis by performing a Fourier transform, *i.e.* $\hat{\psi}(k) = \mathcal{F}[\psi(x)](k)$. Given a time-step of Δt, both can be solved independently:

$$i\partial_t\psi(x,t) = L_1(x,t)\psi(x,t) \qquad \rightarrow \qquad \psi(x,t+\Delta t) = \psi(x,t)\exp\{-iL_1(x,t)\Delta t\}, \tag{5.1}$$

and

$$i\partial_t\hat{\psi}(k,t) = L_2(k,t)\hat{\psi}(k,t) \qquad \rightarrow \qquad \hat{\psi}(k,t+\Delta t) = \hat{\psi}(k,t)\exp\{-iL_2(k,t)\Delta t\}. \tag{5.2}$$

In this step, it is assumed that the time step Δt is sufficiently small for the L_i to be considered constant over the length of the time step. To perform a full time step, it is neccesary to consider both contributions. To take both contribution into account the Strang Splitting Spectral Method (SSSM) is employed. This method relies on the fact that Eqs. (5.1) and (5.2) can be solved independently. A schematic representation of this method is given in figure 5.1.

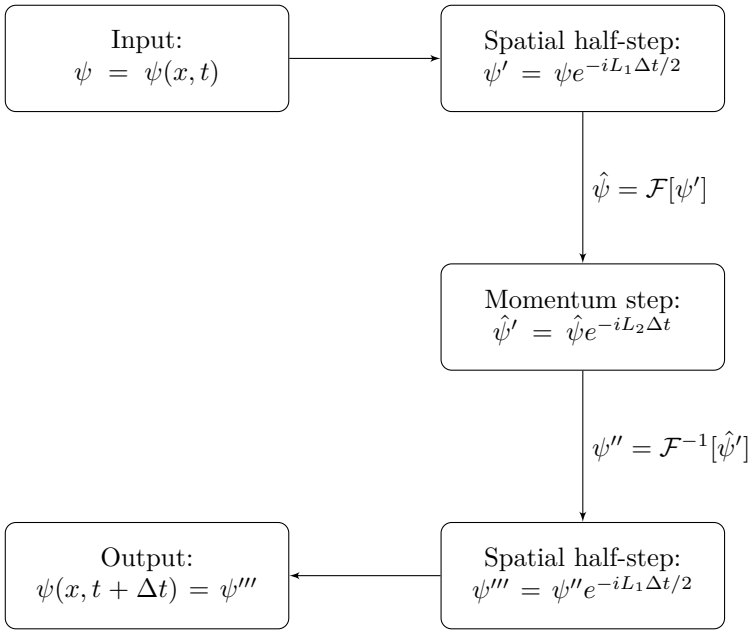

Figure 5.1: Schematic representation of the Strang Splitting Spectral Method.

The SSSM can be applied both to the time evolution and the imaginary time evolution, which is needed to find the ground state. In case of regular time evolution the SSSM is unitary. Timesteps do not change the particle number. It is also inherently stable if time steps are sufficiently small. Also, every grid point update (of which there are three in each time step) in the simulation only relies on the wave function values at this grid point. This allows complete parallelization of each of these updates. This greatly improves speed of the simulation. The Fourier transform can not be computed completely in parallel, but can be sufficiently parallelized to also see a significant speed-up on multiple computing cores.

5.1.1 Finding the ground state

In general, many different configurations of the wavefunction ψ, with a continuous spectrum of energies are possible. However, the ground state for this system is still uniquely determined by the fact that it has the lowest energy. To determine the ground state of the given GPE, imaginary time evolution is used. Imaginary time evolution can be performed by substituting $t \to \tilde{t} = it$. As a result of this substitution, at each time step, all configurations are damped according to their energy, with configurations with larger energy being damped more heavily. By renormalizing after every imaginary time step, it is ensured that no particles are lost. By performing a sufficient number of imaginary time steps the ground state is well-approximated. However, a pure ground state is hard to determine since energy levels are distributed continuously. To converge to the ground state within a small number of steps, the wave function ψ is intialized in the Thomas-Fermi approximation. The Thomas-Fermi approximation is a very good approximation for the spatial profile of the BEC in the experiment. However, it lends itself poorly for numerical simulations.

5.2 Lower simulation dimension

In order to save computation time, the GPE from (3.10) is reduced to two dimensions following the approach in [13]. A full calculation can be found in Appendix B, this subsection will only outline the procedure and discuss the result. In the direction to be integrated out, harmonic trapping is assumed, *i.e.* $U(\mathbf{x}) = W(x,y) + \frac{m\omega_z^2}{2}z^2$. The dimensional reduction is now performed by using a Gaussian Ansatz with variable, position-dependent width and re-deriving the Gross-Pitaevskii equation from the action. The Ansatz for the wave-function is given by

$$\psi_i(\mathbf{x}) = \phi_i(x,y) f_i(z;\eta_i(x,y)) \qquad \text{where} \qquad f_i(z) = \frac{e^{-\frac{z^2}{2\eta_i^2(x,y)}}}{\pi^{1/4}\eta_i(x,y)^{1/2}}.$$

It is assumed that $\eta_1 = \eta_2$ since $g_{11} = g_{12} \approx g_{22}$. It is also assumed that $\nabla^2 f \approx \partial_z^2 f$. By substituting the Ansatz and calculating the Euler-Lagrange equations with respect to ϕ_1^*, ϕ_2^* and η, the dimensionally reduced Euler-Lagrange equations follow. By approximating η in the strong interaction regime, and substituting the result, the dimensionally reduced coupled GPE is found

$$i\hbar\frac{\partial}{\partial t}\begin{pmatrix}\phi_1\\ \phi_2\end{pmatrix} = \left[L_1(x,y;\phi_1(x,y),\phi_2(x,y)) + L_2(\hat{k})\right]\begin{pmatrix}\phi_1\\ \phi_2\end{pmatrix}, \tag{5.3}$$

where

$$L_1(x,y;\phi_1(x,y),\phi_2(x,y)) = \begin{pmatrix}\mathcal{H}_1 & \frac{\hbar\Omega_{\text{eff}}}{2}\\ \frac{\hbar\Omega_{\text{eff}}^*}{2} & \mathcal{H}_2\end{pmatrix} \qquad \text{and} \qquad L_2(\hat{k}) = -\frac{\hbar}{2m}\begin{pmatrix}\nabla_\perp^2 & 0\\ 0 & \nabla_\perp^2\end{pmatrix}. \tag{5.4}$$

The single-component Hamiltonians $\mathcal{H}_i$ are given by

$$\mathcal{H}_i = W(x,y) + \frac{3N^{2/3}}{4\pi^{2/3}\tilde{a}^{1/3}a_z^{4/3}}\frac{\sum_{j=1,2}\tilde{g}_{ij}|\phi_j|^2}{(|\phi_1|^2+|\phi_2|^2)^{1/3}} + \frac{\hbar|\Omega_i|^2}{2\Delta} - \mu. \tag{5.5}$$

Here, $\tilde{a} = \frac{a_{11}+2a_{12}+a_{22}}{4}$, $\tilde{g}_{ij} = \frac{2g_{ij}+\tilde{g}}{3}$, $\tilde{g} = \frac{g_{11}+2g_{12}+g_{22}}{4}$, and $a_z = \sqrt{\frac{\hbar}{m\omega}}$. Note that the interaction term in the Hamiltonian now scales $\propto |\phi|^{4/3}$, while other terms remain the same. This is due to expansion of the atom cloud as a result of repulsive interactions between the atoms in the direction which is integrated out. The equation has also been split in the position-dependent part L_1 and momentum-dependent part L_2, to underline how this equation is used in the SSSM algorithm of the previous section. The matrix is exponentiated to achieve a solution similar to (5.1). A brief discussion of exponentiation of matrices can be found in appendix C.

5.3 Simulation results

Having outlined the numerical methods used to execute the simulation and the theory in a dimensionally reduced system, the simulation can be performed. The simulation is performed for our experimental setup, which has a cigar-shaped symmetry. Table 3 shows the simulation parameters used, which are typical experimental parameters.

Table 3: Parameters used in the simulation, which are typical parameters in the experiment.

Particle number N	10^7
ω_x	$2\pi \times 16\,\mathrm{Hz}$
$\omega_{y,z}$	$2\pi \times 104\,\mathrm{Hz}$
Simulation grid size	3072×512
Physical grid size	$4R_{x,\mathrm{TF}} \times 4R_{y,\mathrm{TF}}$
Time step	$10^{-4}T_{x,\mathrm{HO}}$ (imag. time, dynamics) $2 \times 10^{-5}T_{x,\mathrm{HO}}$ (coupling)

5.3.1 Ground state and convergence

As the experiment involves around atoms starting in a single state, the ground state is determined for a single component. This is done using the imaginary time evolution described in the previous section. For the convergence, the free energy per particle F is studied, which corresponds to the expression for the energy $\mathcal{H}_1$ in Eq. (5.4), including the kinetic term. So

$$F = \mathcal{H}_1 + \frac{\hbar^2 k^2}{2m}.$$

The k^2 part is calculated by taking a Fourier transform of the wavefunction. Figure 5.2 shows the rate of convergence for typical parameters. Convergence seems to start faster than exponential, but as the numerical precision starts playing parts, it slows down. Convergence is achieved within 5000 time steps, which, for given grid sizes corresponds to about 20 to 30 minutes of computation time.

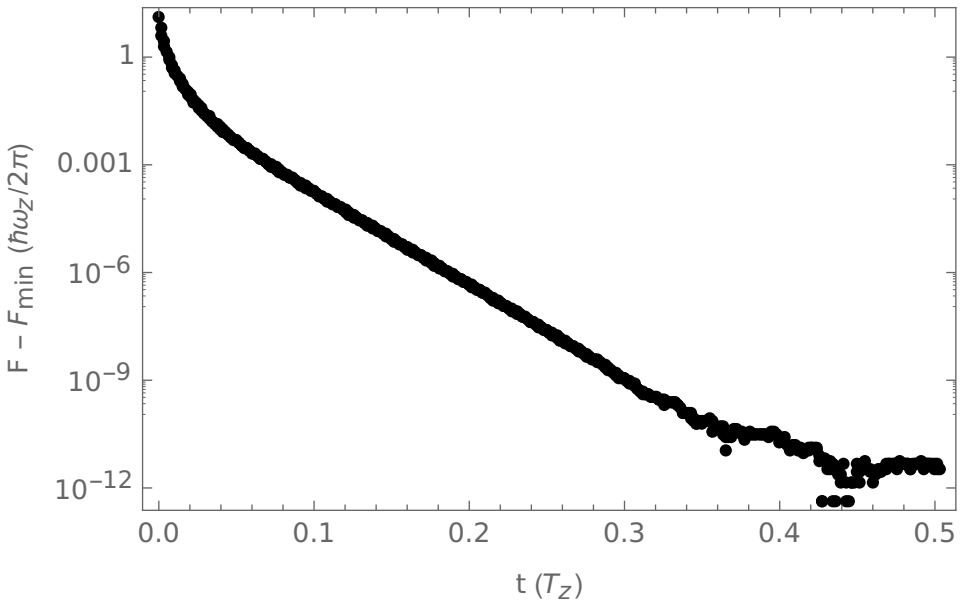

Figure 5.2: This figure demonstrates the convergence during the imaginary time evolution. This figure contains about 500 data points, amounting to a total of 5000 time steps, with one sample every 10 steps. The t-axis is linear in units of $T_z = 2\pi/\omega_z$, where ω_z is the trap frequency. The $F - F_{\mathrm{min}}$-axis is logarithmic and scaled to the energy quantum $\hbar\omega_z/(2\pi)$. Units on axes are the dimensionless units used in the simulation. By $t = 0.5T_z$, the free energy had converged to the numerical precision.

5.3.2 Raman simulation and results

Once in the ground state, time evolution can commence. For the time evolution, both components are considered and coupling is immediately turned on. The Raman parameters used in the simulation are found in table 4. The shaped Rabi frequency Ω_1 is chosen as a homogenous field with a phase winding at the center with a vortex core size chosen of $\zeta = 20\,\mu$m. The time step is significantly reduced, as the contribution from the coupling terms and light shift terms in the Hamiltonian are roughly a factor of 10 to 50 larger than the terms which dominate the dynamics in the absence of coupling.

Table 4: Raman parameters used in the simulation.

Rabi field Ω_1	$\Omega_1(r,\theta) = \begin{cases} \Omega_0 \frac{r}{\zeta} e^{i\phi} & r < \zeta \\ \Omega_0 e^{i\phi} & r > \zeta \end{cases}$
Rabi field Ω_2	$\Omega_2(r,\theta) = \Omega_0$
$\Omega_{\text{eff}} = \frac{\Omega_0^2}{\Delta}$	$2\pi \times 40\,\text{kHz}$
Time step	$2 \times 10^{-5} T_{x,\text{HO}}$

Running the simulation for these parameters takes about 4 hours, during which approximately 3 Raman cycle times ($T_{\text{Raman}} = \frac{2\pi}{\Omega_{\text{eff}}}$) are resolved. In figure 5.3, the fraction of atoms in each component is shown. At $t = 0.5 T_{\text{Raman}}$, approximately 80% of all atoms is transferred to the second state through the Raman coupling. However, due to the finite vortex core size, not all atoms are transferred. In the remainder of the time evolution, it is seen that in the simulation, the occupation numbers of the states oscillate as expected in the case of Raman coupling. In the vortex core, the effective Raman frequency is lower, so flopping between states is slower, which exhibits in the same way as a dephasing effect. However, a large fraction of atoms can be transferred through Raman coupling between the two states.

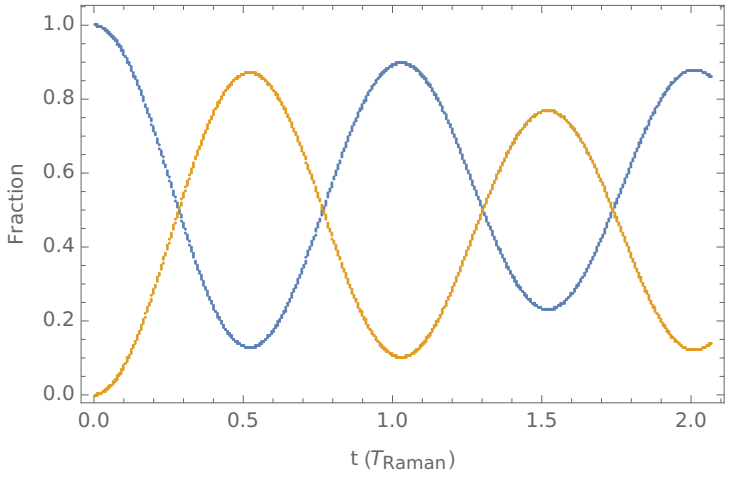

Figure 5.3: Fraction of the atoms in the first component (blue) and the second component (yellow) as a function of time. Note that at $t = 0.5 T_{\text{Raman}}$, not the full amount of atoms is transferred due to the finite vortex core size used in the simulation.

In figure 5.4, the dynamics are illustrated in the way of stills. From this it can be seen that outside of the vortex core atoms are homogeneously transferred back and forth between the two states, while the second component picks up the vortex phase pattern. Near the vortex core, around $t = 0.7\,T_{\text{Raman}}$, it can be seen that due to phase mismatch in the first component a domain wall is formed. This domain wall exhibits as a circular structure in the optical vortex core. The resulting 'free' space is filled with atoms of the second component.

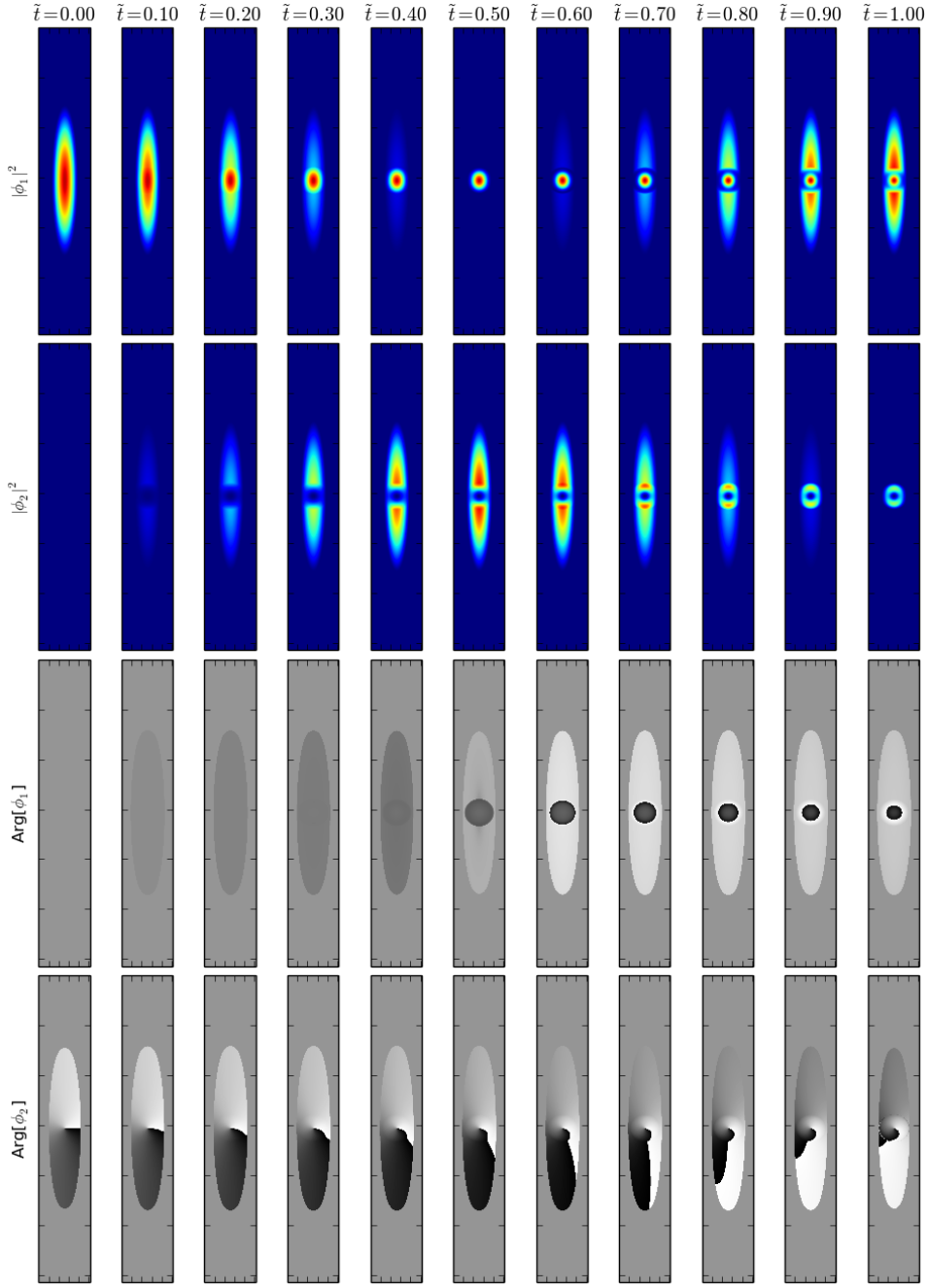

Figure 5.4: Results of the simulation. From top to bottom, there is the density of the first component, density of the second component, phase of the first component and phase of the second component. From left to right, time is shown, where $\tilde{t} = t/T_{\mathrm{Raman}}$.

5.3.3 Conclusion

Simulations indicate that a phase winding in the optical field will result in a phase winding in the phase of the condensed atom cloud. However, due to finite vortex size, the core of this atomic phase winding will be filled with atoms of the other component. By separating the two components using Stern-Gerlach splitting in the experiment, this clear 'core' should be visible.

In the experiment, the second component is not trapped by the magnetic fields and will expand freely upon being transferred. However, time scales in simulations of the coupling are sufficiently short, which permits ignoring the fact that the second component is not trapped.

6 Raman setup and results

This section will discuss the parts of the experimental setup built to perform the Raman coupling between the two states, as well as preliminary measurements where no phase imprinting is performed. The goal is to couple the $(F, m_F) = (1, -1)$ state in which the atoms start to the $(F, m_F) = (1, 0)$ state.

6.1 Raman schemes for sodium

In subsection 3.3, the theory behind Raman coupling is briefly discussed. A three-level Λ-system is considered and the relevant equations are derived. In a physical situation, a pure three-level system can not be considered. In addition to the two groundstates, one has to consider multiple upper states. For the intended transition, there are two schemes using $3^2P_{3/2}$ transitions. It is possible to use the $m_{F'} = 0$ upper states (figure 6.1.a) or the $m_{F'} = -1$ upper states (figure 6.1.b).

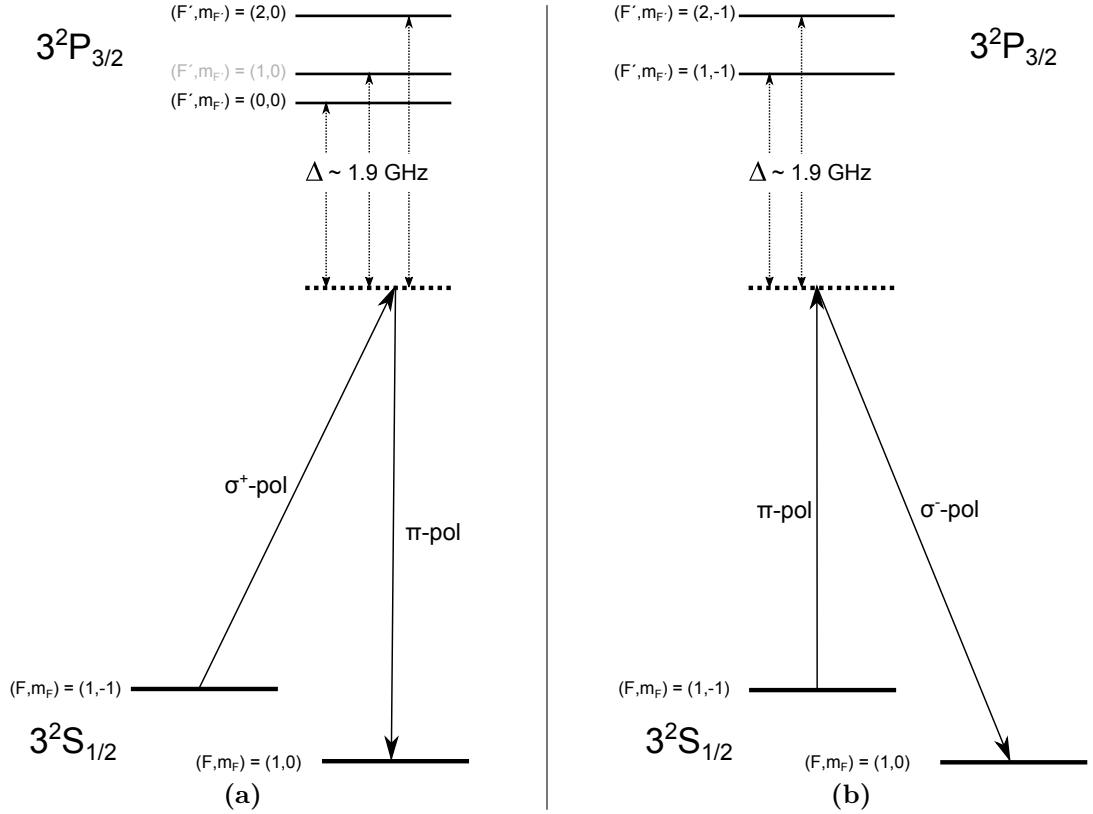

Figure 6.1: Possible transition schemes for a two-photon coupling between the $(F, m_F) = (1, -1)$ and $(F, m_F) = (1, 0)$ states. Due to the large detuning compared to the upper level splitting, $\Delta = 1.9\,\text{GHz}$ is set for all upper levels.. **(a)** Possible transitions using the $m_{F'} = 0$ upper levels. The $(1, 0) \rightarrow (1, 0)$ transition is grayed out because it is not allowed. **(b)** Possible transitions using the $m_{F'} = -1$ upper levels.

Using the bundle paths available in the setup, it is only possible to project light on the atoms perpendicular to the magnetic quantization axis. A basis for linear polarizations is chosen. The light polarized along the quantization axis is referred to as π-polarized. The light polarized perpendicular to the quantization axis is denoted by l_y and can be decomposed as

$$l_y = \frac{\sigma^+ + \sigma^-}{\sqrt{2}}.$$

With this information, it is possible to use either transition scheme of figure 6.1, albeit with only half of the light being effectively used to perform the transition for the transitions where $\sigma^{\pm}$-polarized light is needed.[6]

[6] $\sigma^{\pm}$ polarized light is light is left-/right-handed circularly polarized light, propagating along the magnetic quantization axis.

6.1.1 Calculating Ω_{eff}

As in the case of section 3.3, an effective Rabi frequency Ω_{eff} can be calculated. To do this, one needs to take into consideration the contribution of each level to the population transfer rate. For a system with two ground states ψ_{g_i} and two excited states ψ_{e_i}, $i = 1, 2$, the Hamiltonian from Eq. 3.5 can be extended to include the second upper level. This yields

$$\mathcal{H} = \frac{\hbar}{2}\begin{pmatrix} 0 & \Omega_1^* & \Omega_{1'}^* & 0 \\ \Omega_1 & 2\Delta & 0 & \Omega_2 \\ \Omega_{1'} & 0 & 2\Delta & \Omega_{2'} \\ 0 & \Omega_2^* & \Omega_{2'}^* & 0 \end{pmatrix} \qquad \text{on spinor} \qquad \Psi' = \begin{pmatrix} \psi_{g_1} \\ \psi_{e_1} \\ \psi_{e_2} \\ \psi_{g_2} \end{pmatrix}. \tag{6.1}$$

The detuning with respect to the two upper states is chosen to be Δ since the level splitting of the upper states is small compared to the detuning. The Rabi frequencies denoted with a primed index (*i.e.* $\Omega_{1'}$) are the Rabi frequencies associated with transitions to the second excited state. Using the adiabatic approximation, $\partial_t \psi_{e_i} = 0$, $i = 1, 2$ yields

$$\mathcal{H} = \frac{\hbar}{2\Delta}\begin{pmatrix} |\Omega_1|^2 + |\Omega_{1'}|^2 & \Omega_1^*\Omega_2 + \Omega_{1'}^*\Omega_{2'} \\ \Omega_1\Omega_2^* + \Omega_{1'}\Omega_{2'}^* & |\Omega_2|^2 + |\Omega_{2'}|^2 \end{pmatrix} \qquad \text{on spinor} \qquad \Psi' = \begin{pmatrix} \psi_{g_1} \\ \psi_{g_2} \end{pmatrix}. \tag{6.2}$$

From this, we can derive that an effective Rabi frequency between the two ground states is given by

$$\Omega_{\text{eff}} = \frac{\Omega_1^*\Omega_2 + \Omega_{1'}^*\Omega_{2'}}{\Delta}. \tag{6.3}$$

Since the detuning Δ is approximated to be the same for both transitions, and since the transitions are driven by the same laser beams, such that the electric fields are the same, the above can be written in terms of electric fields and dipole moments as

$$\Omega_{\text{eff}} = \frac{\mathcal{E}_1\mathcal{E}_2}{\Delta\hbar^2}\left[(\vec{\mu}_2 \cdot \hat{e}_2)(\vec{\mu}_1 \cdot \hat{e}_1) + (\vec{\mu}_{2'} \cdot \hat{e}_2)(\vec{\mu}_{1'} \cdot \hat{e}_1)\right]. \tag{6.4}$$

In the above, $\mathcal{E}_i$ indicate electric field amplitudes, $\vec{\mu}_i$ indicate dipole moments, where primed indices refer to dipole moments corresponding to transitions to the second excited state. The polarization vectors for the electric field are given by $\hat{e}_i$. Using this formula, it is straightforward to calculate the effective Raman frequency. The dipole moments for the relevant transitions can be found in table 5.

Table 5: Dipole moments of the transitions relevant to the experiment, as a fraction of the cycling transition ($|F = 2, m_F = 2\rangle \to |F' = 3, m_{F'} = 3\rangle$) dipole moment $\mu_{\text{cyc}} = 2.11305(71) \times 10^{-29}\,\text{C m}$. Data from [8].

σ^- polarized	**π polarized**
$\lvert 1,0\rangle \to \lvert 1,-1\rangle$: $-\sqrt{\frac{5}{12}}$	$\lvert 1,-1\rangle \to \lvert 1,-1\rangle$: $-\sqrt{\frac{5}{12}}$
$\lvert 1,0\rangle \to \lvert 2,-1\rangle$: $\sqrt{\frac{1}{4}}$	$\lvert 1,-1\rangle \to \lvert 2,-1\rangle$: $-\sqrt{\frac{1}{4}}$
σ^+ polarized	$\lvert 1,0\rangle \to \lvert 0,0\rangle$: $\sqrt{\frac{1}{3}}$
$\lvert 1,-1\rangle \to \lvert 0,0\rangle$: $\sqrt{\frac{1}{3}}$	$\lvert 1,0\rangle \to \lvert 1,0\rangle$: 0
$\lvert 1,-1\rangle \to \lvert 1,0\rangle$: $\sqrt{\frac{5}{12}}$	$\lvert 1,0\rangle \to \lvert 2,0\rangle$: $-\sqrt{\frac{1}{3}}$
$\lvert 1,-1\rangle \to \lvert 2,0\rangle$: $\sqrt{\frac{1}{12}}$	

Choosing the proper polarizations for each beam, the effective Rabi frequencies can be calculated by taking the product of the coefficients from table 5. For both schemes in figure 6.1, the effective Rabi frequency is given by

$$\Omega_{\text{eff}} = \frac{\mathcal{E}_1\mathcal{E}_2}{\Delta\hbar^2}\frac{\mu_{\text{cyc}}}{12}. \tag{6.5}$$

The factor of 1/6 is a result of the coefficients in table 5 and an extra factor of 1/2 enters because one of the electric fields effictively only contributes half. This is because $\sigma^{\pm}$-polarization is needed, but only light polarized linearly to the quantization axis can be used. In both schemes, the two terms involving the dipole moments are of opposite sign, indicating the two paths interfere destructively with each other.

6.2 Raman setup

To obtain Raman coupling between two states, two laser beams are needed at a frequency difference Δf equal to the level spacing between the two levels which will be coupled. To obtain light with a large detuning Δ compared to the hyperfine splitting of the $3^2P_{3/2}$ states, light from the slowing laser is used. This light is detuned approximately $\Delta = 1.9\,\text{GHz}$ from the $F_g = 1$ to $3^2P_{3/2}$ transitions. The frequency difference between the two spin states $\Delta f \approx 3\,\text{MHz}$ is obtained by driving the AOM in one beam with a constant frequency of 80.00 MHz while the AOM in the other beam has its drive frequency supplied by a direct digital synthesizer (DDS) and is tuned at a frequency $80\,\text{MHz} - \Delta f$. Using the DDS, the frequency difference between the two AOMs can be tuned up to a kilohertz. An overview of the setup on the laser table can be seen in figure 6.2. To provide sufficient light, a foldable mirror mount is used to insert a $\lambda/2$ waveplate in the laser beam before the Zeeman slower PBS. This way, the light which enters the Zeeman slower path during the laser cooling sequence can be used for the Raman beams during the experiment.

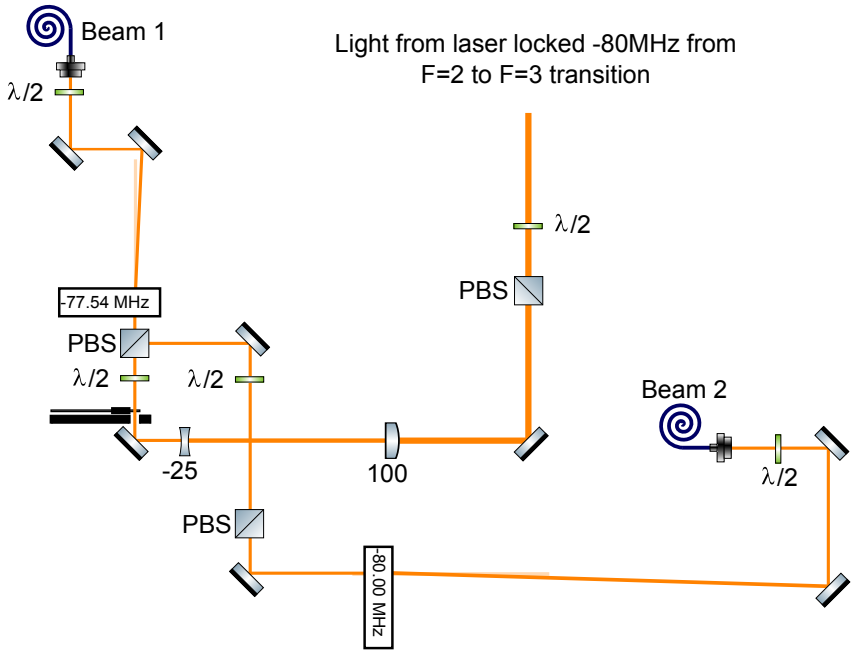

Figure 6.2: Branch of the laser table dedicated to generating the Raman beams. An outtake from figure 2.2.

In the experimental setup the beams are coupled out using lensless out-couplers and a cage-mounted achromatic lens ($f = 45\,\text{mm}$) to provide two nearly Gaussian beams with a diameter of approximately 25 mm. One beam is passed over the SLM while the other is input directly into a beamsplitter cube, which is used to combine to overlap the two beams. To project the light into the setup, the same achromatic lens ($f = 200\,\text{mm}$) is used as is used to collimate the probe beam which is used to image the atoms. This has the disadvantage of having to use two 50/50 beamsplitters: one to overlap the beams and one to mix the light with the probe light. However, it is possible to use the camera which is used to image the atoms, to image the SLM directly. By doing this, it is possible to adjust the position of the SLM such that it is sharply imaged on to the atoms, which is a requirement for the experiment. An overview of the SLM setup is given in figure 6.3. The distance from the final mirror to the atoms is approximately 300 mm. The distance from the lens to the SLM is approximately 600 mm. This yields an magnification of 0.5. The ideal imaging resolution due to the backplane numerical aperture is 7 μm.

6.3 Effect of single beams

Before moving on to attempting the two-photon Raman coupling, the effect of both beams individually is studied. In these exploratory measurements effects are observed which will distort the signal in the final

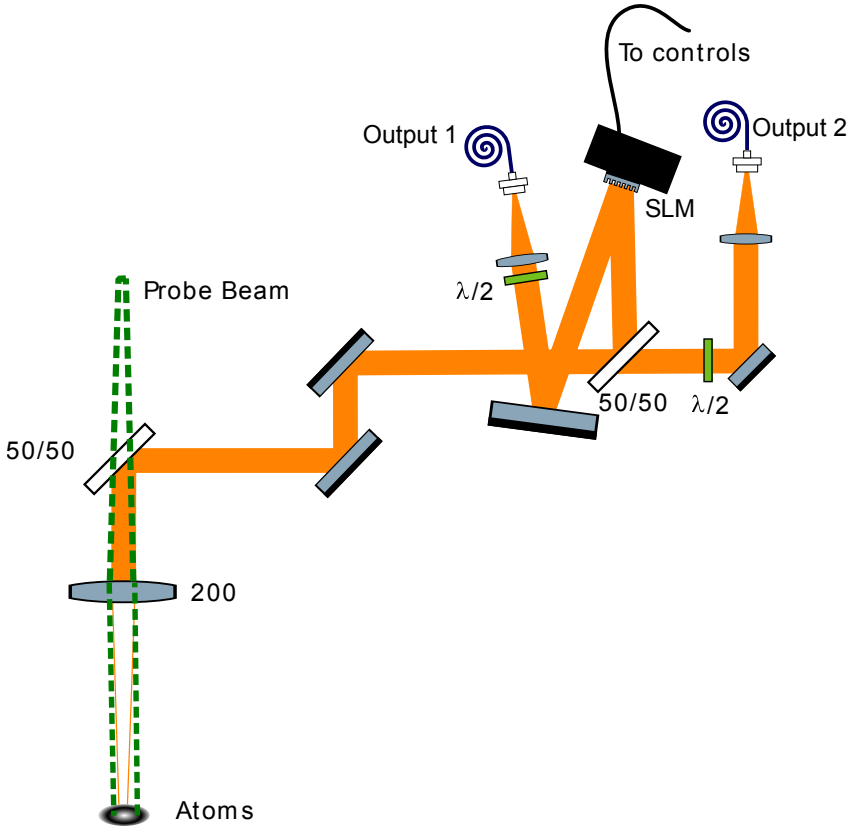

Figure 6.3: Optics setup used to project the Raman beams on to the atoms.

experiment. Firstly, due to reflection on different optical elements, there is a 2-photon transition using the reflected light. Secondly, a coherent collective excitation, referred to as superradiance, is excited.

6.3.1 Reflected light

Due to other experiments in the lab, there is a beam path to project a beam from the bottom which is focussed exactly at the center of the atom cloud. This beam path also contains a fiber outcoupler similar to the ones shown in figure 6.3. Due to reflections on the fiber head, a beam which is counter-propagating to the Raman beams is obtained. This beam allows a two-photon transition to the upper state and back. The signature for this transition is the transfer of two photon momenta. This phenomenon is observed using an alternative beam path, which makes an 45° angle to the original probe beam and is used for quantative measurements during the evaporative cooling process. The experimental signature for this entire process in shown in figure 6.4. Once the problem was identified, secondary, unused beam paths were blocked. This suppresses reflections sufficiently and the effect is no longer observed.

6.3.2 Superradiance

In cylindrically shaped Bose-Einstein condensates the coherence of the system strongly correlates subsequent Rayleigh scattering events [14]. Every atom undergoing Rayleigh scattering will increase the likeliness of Rayleigh scattering in the same direction even further, causing exponential gain with illumination time. This effect is suppressed for light polarized parallel to the long axis of the cylinder, but is a strong effect for light polarized perpendicular to this long axis[7]. The experimental signature for superradiance is shown in figure 6.5. This image is made along the imaging axis which makes an 45° angle to the probe and Raman beams. Supressing this effect can be done by choosing a short illumination time. Also, the power in the Raman beams can be imbalanced to suppress the superradiance following from light polarized perpendicular

[7]The long axis of the cylinder coincides with the quantization axis of the magnetic field.

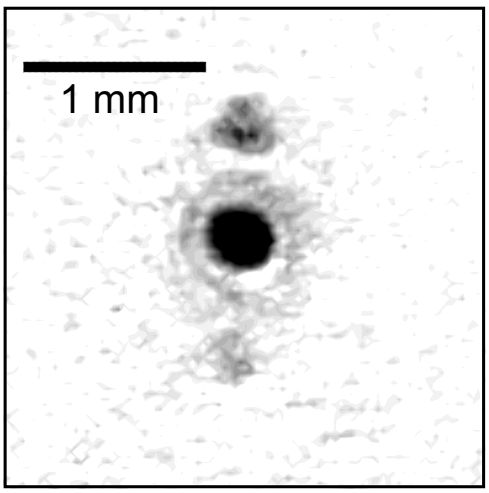

Figure 6.4: Experimental signature of a two-photon transition with back-reflected light. The displacement of the two additional clouds correspond to two photon momenta. Time of flight is 20 ms.

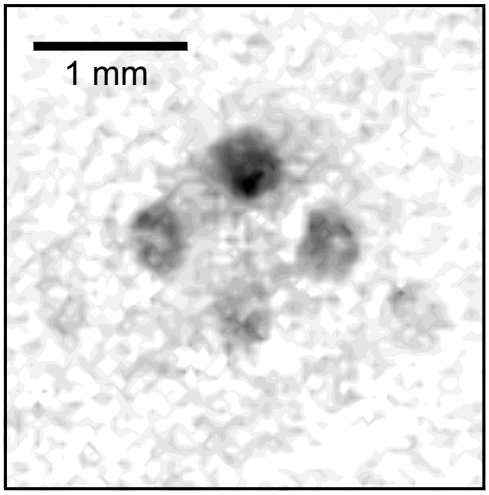

Figure 6.5: Experimental signature of superradiance. The diagonal displacement corresponds to a horizontal plus vertical photon momentum. Multiple nodes are seen, corresponding to multiple scattering events. Time of flight is 20 ms.

6.4 Preliminary results

Before moving to phase imprinting, an experiment without a pattern on the SLM is run. In the experiment, the scheme of 6.1.b is used. Both beams are approximately Gaussian. The intensity of both beams at the atoms is determined to be $I_1 = 53\,\mathrm{W/m^2}$ and $I_2 = 141\,\mathrm{W/m^2}$. The beams are chosen to be of unequal intensity to suppress superradiance. The given intensities lead to an effective Rabi frequency of $\Omega_{\mathrm{eff}} = 2\pi \times 3,\mathrm{kHz}$. After the Raman transfer, the magnetic fields are immediately turned off and a total time of flight of 20 ms is used. To separate the different spin states the MOT magnetic fields are kept on for 10 ms. The result of a measurement with an illumination time of $\tau = 10\,\mu\mathrm{s}$ with the Raman beams is shown in figure 6.6.a. Comparing the illumination time to the effective Rabi frequency yields $10\,\mu\mathrm{s} \approx 0.05 \times 2\pi/\Omega_{\mathrm{eff}}$, implying nearly no population should be transferred. However, population transfer is observed. From a rudimentary fit shown in figure 6.6.b, it follows that the population is divided over the components as fractions $(f_{-1}, f_0, f_1) = (0.31, 0.48, 0.21)$. Not only is population transferred from the $m_F = -1$ to the $m_F = 0$ state, but population is also transferred to the $m_F = 1$ state. Since the level splitting between $m_F = 0$ and $m_F = 1$ is nearly equal to the splitting between $m_F = -1$ and $m_F = 0$, coupling between these levels is expected.

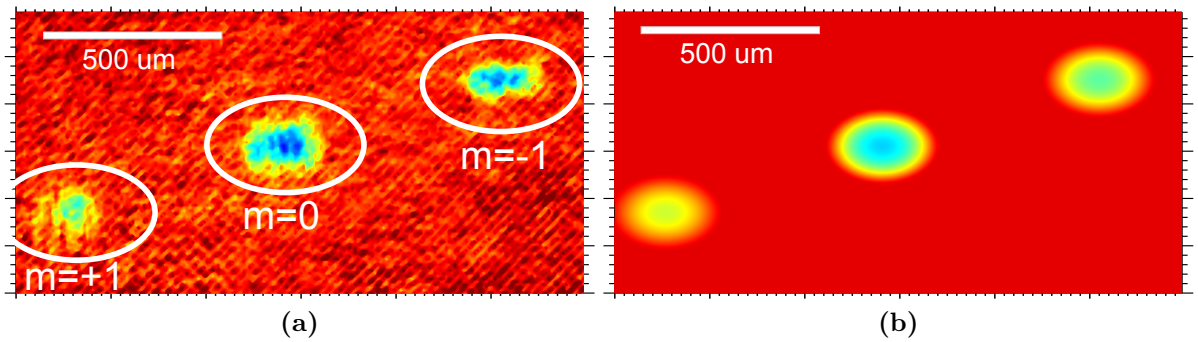

Figure 6.6: Figure demonstrating Raman coupling between $m_F = -1, 0, 1$ states. **(a)** Experimental data with spin projection m_F indicated in the figure. Some spatial deformation of the atom cloud is observed. **(b)** Fit to the data of (a) using a Thomas-Fermi profile.

In figure 6.6 it is observed that the spatial profile of the atom cloud does not resemble that of a Thomas-Fermi profile anymore. This is the result of the interaction with the light and is seen even when one of the beams is off, but appears most clear when atoms are transitioned to another state. The cause for

the distortion has not been determined yet, but it is possible that this is (partly) due to the fact that atoms of different species with inequal scattering lengths tend to form domains. This would imply the patterns observed are due to magnetic domains forming during the transfer and seperation.

6.4.1 Discussion

During the experiment described in this section stability of the magnetic fields is very important. The single-photon detuning δ, defined as $\delta = \Delta_1 - \Delta_2$ where Δ_1 and Δ_2 are those of figure 3.1, is typically 50 kHz for these experiments. Thus fluctuations in the magnetic fields causing a 100 kHz shift in the magnetic splitting between the levels seriously complicates reproducibility. At the time the measurements of this section were taken, stability of the magnetic trapping fields were a problem, leading to irreproducable results.

In the experiment a lot of light is needed to perform the two-photon transition. This leads to problems with effects such as superradiance. The fact that the two contributions from the upper states interfere destructively is the main cause a lot of light has to be used. Using a different transition scheme may provide the best option to reduce the amount of light used.

6.5 Recommendations

Based on the results of the preliminary measurements, it is advisable to choose another transition scheme. A good candidate is coupling the $m_F = -1$ and $m_F = +1$ states, as seen schematicly in figure 6.7. The same setup as has been used for this measurement can also be used with this modified transition scheme. The only difference is that the DDS which drives the second AOM has to be set for $\Delta f \approx 6\,\text{MHz}$ and the light polarizations have to be changed accordingly.

This new transition scheme has benefits and downsides. The major benefit is that the upper levels all interfere constructively, leading to an effective Raman frequency which is 10 times larger than the one used in the preliminary measurements. The major downside is that both beams have to be polarized to provide $\sigma^{\pm}$-polarized light, which means both can effectively only be utilized half for the coupling. However, even while taking this into account, the effective Raman frequency will still be 2.5 times larger than in the preliminary measurements.

The polarization of light dictated by this transition scheme matches that needed for superradiance. However, since less light is needed to obtain the same Raman frequency, shorter illumination times or lower power can be used. Alternatively, one can decompress the trap in the radial direction to get a more spherical geometry, to suppress superradiance even more.

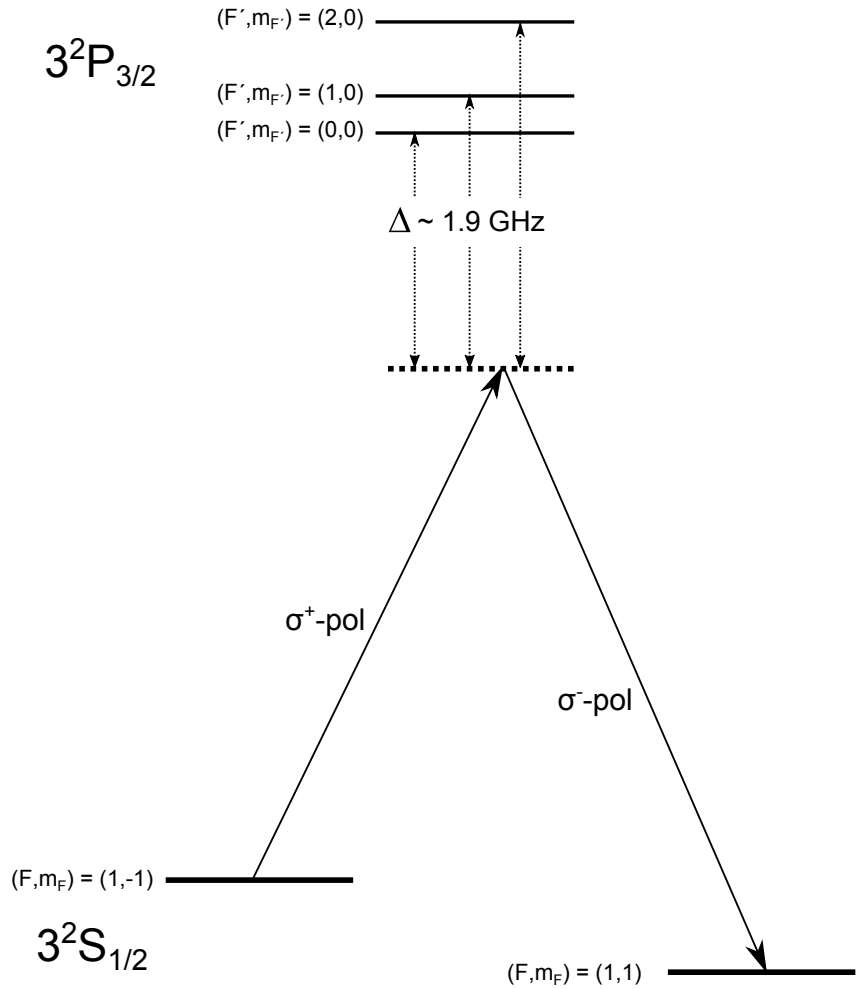

Figure 6.7: Transition scheme to obtain a two-photon coupling between the $m_F = -1$ and $m_F = 1$ states of the $F = 1$ ground state.

Acknowledgments

Research, especially experimental research, is not something you do alone. Work is done in a research group and everyone puts in effort to do the experiments attributed to the inviduals writing them down in their thesis. I would like to thank my fellow students and lab mates first and foremost. Broos, Qiao, Koen and Charly. Thank you for the work you put in to help me, for being there to bounce ideas off of and for our cooperation. Aside from my direct lab mates, I'd like to thank all the people at the Nanophotonics group for their moral support and the fun we've had.

Thanks go to the technicians as well. Cees, Frits, Dante and Paul for their technical support and the many things which they have made for us, trying to meet deadlines which sounded like 'Preferably this afternoon, but actually I already needed it yesterday.' Thanks also to my supervisor professor Peter and doctor Dries for the fruitful discussions and the fact that I am (nearly) always able to crash into their offices and send a barrage of questions their way, which are always answered.

Writing a thesis is not just an academic feat. It is also taxing on your personal life. Therefore I would like to mention my roommates at Warande 103 and my family. Thanks for putting up with me guys, when things in the lab were going sour and I was extremely moody. The person who probably had to deal most with my moods was Zoë. Thank you for your support and love and dealing with me.

A Release-recapture measurements

To determine the temperature of the MOT, release-recapture measurements were performed. In release-recapture measurements, MOT beams are briefly turned off, then on again to determine the fraction of atoms which is recapture by the MOT beams. From this fraction, the temperature can then be estimated.

A.1 Experimental method

To determine the temperature, the fluorescence for different recapture times Δt has to be determined. The MOT is loaded as usual. After loading is completed, the Zeeman slower laser and atom beam are blocked. The MOT beams are then turned off for a time Δt. After the MOT beams are turned on, the atoms are recaptured. During the release and recapture, the total intensity of the MOT is captured on a power meter. The time $t = 0$ is chosen to coincide with the moment the MOT beams are turned off. The recapture curve is fitted by an exponential decay $\propto I_e e^{-t/\tau} + I_0$. A sample measurement can be seen in figure A.1.

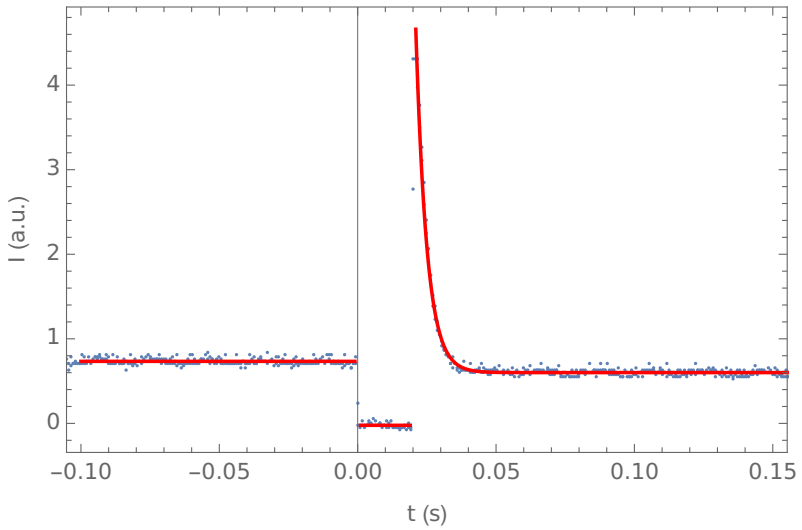

Figure A.1: Typical release-recapture measurement. Blue point are data while the red line is a fit. The off-time Δt is characterized by the near-zero intensity. For this measurement $\Delta t = 20\,\text{ms}$.

From this figure, three data points are extracted: the MOT fluorescence before recapture, the background light and the MOT fluorescence after recapture. The first is determined at $t < 0$, the second is determined from the line between $t = 0$ and $t = \Delta t$ and the third is determined from the flat line after exponential decay. From this, the normalized recaptured fraction can be determined.

To determine the temperature, the MOT is assumed to be spherical with some recapture radius R_c and at thermal equilibrium at some temperature T. The speed at which atoms will have to travel to escape the capture volume is given by the capture velocity $v_c = R_c/\Delta t$. Thus, by calculating the fraction of atoms which have a velocity lower than the recapture velocity, the recapture fraction can be determined. The result is

$$f_r = \frac{4}{\pi^{1/2}} \int_0^{v_c/v_T} \mathrm{d}u\, u^2 e^{-u^2}, \tag{A.1}$$

where $v_T = \sqrt{\frac{2k_B T}{m}}$ is the thermal velocity. Evaluating this expression yields

$$f_r = -\frac{v_c}{v_T} \frac{2e^{-v_c^2/v_T^2}}{\pi^{1/2}} + \mathrm{Erf}\left[\frac{v_c}{v_T}\right], \tag{A.2}$$

where $\mathrm{Erf}[x]$ indicates the error function. Equation (A.2) makes it possible to determine the temperature from the remaining fraction.

A.2 Results

The release-recapture experiment was performed for Δt between 2 ms and 50 ms, with a step size of 2 ms. The recapture radius was estimated by considering the dimensions of the MOT laser beams. Since the MOT beam in the longitudinal trap direction is slightly smaller, a geometrical average of the three beam radii was chosen, resulting in $R_c = 1.6\,\text{cm}$. The results of the entire release-recapture measurement is shown in figure A.2. The temperature was determined to be $717 \pm 33\,\mu\text{K}$. The listed uncertainty followed from the fit. However, temperatures determined in this way are inaccurate, as the temperature depends quadratically on the recapture radius R_c, which can not accurately be determined.

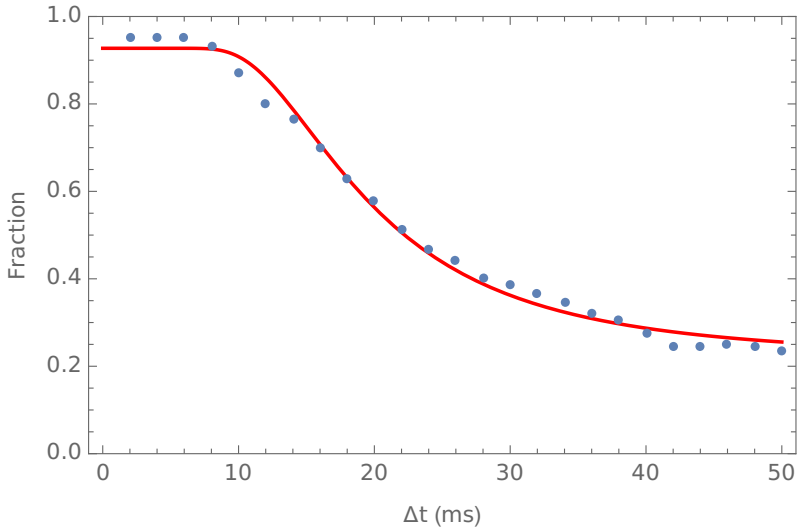

Figure A.2: Results of the MOT release-recapture measurements. The blue dots indicate measurements, while the red line indicates the model of Eq. (A.2). The determined temperature is $\sim 700\,\mu\text{K}$.

B Dimensional reduction

In this appendix the details of the dimensional reduction will be discussed. The starting point is the action of Eq. (3.9). This action is cut into parts which will be treated one at each time. Thus

$$S_{\text{coupled}}[\Psi] = \int \mathrm{d}^3x\, \mathrm{d}t\{\mathcal{L}_{\text{time}} + \mathcal{L}_1[\psi_1] + \mathcal{L}_2[\psi_2] + \mathcal{L}_{\text{coup}}\},$$

where

$$\mathcal{L}_{\text{time}}[\Psi] = \Psi^\dagger i\hbar\partial_t\Psi, \tag{B.1}$$

$$\mathcal{L}_i[\psi_i] = \frac{\hbar^2}{2m}\psi_i^*\nabla^2\psi_i - W_i(x,y)|\psi_i|^2 - \frac{m\omega_z^2}{2}z^2|\psi_i|^2 - \frac{N}{2}(g_{ii}|\psi_i|^4 + g_{ij}|\psi_i|^2|\psi_j|^2), \tag{B.2}$$

$$\mathcal{L}_{\text{coup}} = \frac{|\Omega_1|^2}{2\Delta}|\psi_1|^2 + \frac{|\Omega_2|^2}{2\Delta}|\psi_2|^2 + \frac{1}{2}\left(\psi_1^*\Omega_{\text{eff}}\psi_2 + \psi_2^*\Omega_{\text{eff}}^*\psi_1\right), \tag{B.3}$$

where $j \neq i$ in the second equation. Along the lines of [13], a Gaussian Ansatz is used for the z direction. In the low particle number regime, the ground state of the BEC will be the ground state of the harmonic oscillator, while in the high particle number regime, the interactions are strong and the BEC ground state is generally not Gaussian, but this Ansatz is still able to make accurate predictions. Thus for ψ_i we substitute

$$\psi_i(\mathbf{x},t) = \phi_i(x,y,t)f(z;\eta(x,y)) \qquad \text{where} \qquad f(z;\eta(x,y) = \frac{\exp\left(-\frac{z^2}{2\eta^2(x,y)}\right)}{\pi^{1/4}\eta(x,y)^{1/2}}.$$

The function f is normalized when integrated over z, while ϕ_i $(i = 1,2)$ is normalized such that $\int \mathrm{d}^2x(|\phi_1|^2 + |\phi_2|^2) = 1$. Substituting this in the non-coupling terms, and approximating $\nabla f = \partial_z f$, yields

$$\begin{aligned}\mathcal{L}_i[\psi_i] =& \frac{\hbar^2}{2m}\left(\phi_i^*\nabla_\perp^2\phi_i - \frac{|\phi_i|^2}{\eta_i^2} + \frac{z^2}{\eta_i^4}|\phi_i|^2\right)|f_i|^2 - W(x,y)|\phi_i|^2|f|^2 - \frac{m\omega_z^2}{2}|\phi_i|^2|f_i|^2 \\ & - \frac{N}{2}\left(g_{ii}|\phi_i|^4|f_i|^4 + 2g_{ij}|\phi_i|^2|f_i|^2|\phi_j|^2|f_j|^2\right).\end{aligned}$$

To integrate out the z direction, the following integrals are used:

$$\int \mathrm{d}z\, |f_i|^2 = 1, \qquad \int \mathrm{d}z\, z^2|f_i|^2 = \frac{\eta_i^2}{2},$$

$$\int \mathrm{d}z\, |f_i|^2|f_j|^2 = \frac{1}{\sqrt{\pi(\eta_i^2+\eta_j^2)}}, \qquad \int \mathrm{d}z\, f_i^* f_j = \sqrt{\frac{2\eta_i\eta_j}{\eta_i^2+\eta_j^2}}.$$

Using these integrals, the result is

$$\mathcal{L}_i[\psi_i] = \phi_i^*\left\{\frac{\hbar^2}{2m}\nabla_\perp^2 - W(x,y) - \frac{N}{2}\left(\frac{g_{ii}}{\sqrt{2\pi}\eta_i}|\phi_i|^2 + \frac{2g_{ij}}{\sqrt{\pi(\eta_i^2+\eta_j^2)}}|\phi_j|^2\right) - \frac{\hbar^2}{4m}\eta_i^{-2} - \frac{m\omega_z^2}{4}\eta_i^2\right\}\phi_i \tag{B.4}$$

and for the coupling part of the action it is found that

$$\mathcal{L}_{\text{coup}} = \frac{|\Omega_1|^2}{2\Delta}|\phi_1|^2 + \frac{|\Omega_2|^2}{2\Delta}|\phi_2|^2 + \frac{1}{2}\sqrt{\frac{2\eta_1\eta_2}{\eta_1^2+\eta_2^2}}\left(\phi_1^*\Omega_{\text{eff}}\phi_2 + \phi_2^*\Omega_{\text{eff}}^*\phi_1\right), \tag{B.5}$$

For the time dependent part $\psi \to \phi$ is the only change. Now, since $g_{11} = g_{12} = 0.96g_{22}$, $\eta_1 = \eta_2$ is approximated, since the exact value of the η variable is not relevant to the two-dimensional dynamics

studied in this experiment. Now the Euler-Lagrange equations with respect to η and $\Phi^\dagger = (\phi_1^*, \phi_2^*)$ can be derived. Starting with the equation for η:

$$\frac{\delta S}{\delta \eta} = \left(\frac{\hbar^2}{2m} \eta^{-3} - \frac{m\omega_z^2}{2} \eta \right) \left(|\phi_1|^2 + |\phi_2|^2 \right) + \frac{N\eta^{-2}}{2\sqrt{2\pi}} \left(g_{11}|\phi_1|^4 + 2g_{12}|\phi_1|^2|\phi_2|^2 + g_{22}|\phi_2|^4 \right) = 0. \quad \text{(B.6)}$$

Setting all interaction parameters g equal to $\tilde{g} = \frac{g_1 1 + 2g_{12} + g_{22}}{4}$ using the same argument used to set the η equal, and discarding the "momentum" term $\frac{\hbar^2 \eta^{-3}}{2m}$ since the experiment is in the strongly interacting regime, the equation is easily solved for η, the result is

$$\eta = \left\{ N\tilde{a} a_z^4 2^{3/2} \sqrt{\pi} \left(|\phi_1|^2 + |\phi_2|^2 \right) \right\}^{1/3}, \quad \text{(B.7)}$$

where $\tilde{a} == \frac{a_{11} + 2a_{12} + a_{22}}{4}$ is the averaged scattering length and $a_z = \sqrt{\frac{\hbar}{m\omega_z}}$ is the harmonic oscillator length. Now the Euler-Lagrange equation for $\Phi^\dagger$, with the result for η substituted, yields:

$$i\hbar \frac{\partial}{\partial t} \begin{pmatrix} \phi_1 \\ \phi_2 \end{pmatrix} = \begin{pmatrix} \mathcal{H}_1 & \frac{\hbar \Omega_{\text{eff}}}{2} \\ \frac{\hbar \Omega_{\text{eff}}^*}{2} & \mathcal{H}_2 \end{pmatrix} \begin{pmatrix} \phi_1 \\ \phi_2 \end{pmatrix}, \quad \text{(B.8)}$$

where

$$\mathcal{H}_i = -\frac{\hbar^2}{2m} \nabla_\perp^2 + W(x,y) + \frac{3N^{2/3}}{4\pi^{2/3} \tilde{a}^{1/3} a_z^{4/3}} \frac{\sum_{j=1,2} \tilde{g}_{ij} |\phi_j|^2}{(|\phi_1|^2 + |\phi_2|^2)^{1/3}} + \frac{\hbar |\Omega_i|^2}{2\Delta} - \mu.$$

This equation corrosponds to (3.10). Note that $\tilde{g} = \frac{g_{11} + 2g_{12} + g_{22}}{4}$, while $\tilde{g}_{ij} = \frac{2g_{ij} + \tilde{g}}{3}$, showing the fact that the interaction parameter along the z direction is averaged.

It is interesting to note that this theory may just as easily be applied to reduce a system to a single dimension, which would suit our experimental setup with its cylindrical dimension better. However, since vorticity is the subject of this study, the choice is to only integrate out one direction here.

C Exponentiation of matrices

In this appendix, a brief overview of solving 2-component linear systems is given, using matrix exponentiation. When solving coupled linear differential equations of two variables, one runs into equations of the form

$$\partial_t \begin{pmatrix} f(t) \\ g(t) \end{pmatrix} = \begin{pmatrix} a & c^* \\ c & b \end{pmatrix} \begin{pmatrix} f(t) \\ g(t) \end{pmatrix}, \tag{C.1}$$

where the matrix is chosen to be Hermitian, in correspondence with a Hamiltonian matrix. The parameters a, b, c are complex constants and f and g are complex functions. In the one-dimensional case, this type of equation is trivially solved. The result being given in equation (C.2):

$$\partial_t f(t) = \alpha f(t) \qquad \rightarrow \qquad f(t) = f(t_0) e^{\alpha(t-t_0)}. \tag{C.2}$$

In the two-dimensional case, the solution is equivalent. By writing

$$\overrightarrow{\overrightarrow{A}} = \begin{pmatrix} a & c^* \\ c & b \end{pmatrix} \qquad \text{and} \qquad \vec{v}(t) = \begin{pmatrix} f(t) \\ g(t) \end{pmatrix}$$

the equation can be written as

$$\partial_t \vec{v}(t) = \overrightarrow{\overrightarrow{A}} \vec{v}(t). \tag{C.3}$$

Expanding the one-parameter solution into a power series, the same result can be used here to determine a solution, yielding

$$\vec{v}(t) = \left(\sum_{k=0}^{\infty} \frac{\overrightarrow{\overrightarrow{A}}^k}{k!} (t-t_0)^k \right) \vec{v}(t_0). \tag{C.4}$$

The power series represents the exponent of the matrix. This form can be reduced further by using the fact that the power series is that of the exponent function. Let $\overrightarrow{\overrightarrow{B}} = \overrightarrow{\overrightarrow{A}}(t-t_0)$. If we assume for a moment that $c = 0$, such that $\overrightarrow{\overrightarrow{B}}$ is a diagonal matrix, it is seen that

$$\overrightarrow{\overrightarrow{B}}^k = \begin{pmatrix} a^k (t-t_0)^k & 0 \\ 0 & b^k (t-t_0)^k \end{pmatrix}.$$

By using this fact, we can immediately write

$$e^{\overrightarrow{\overrightarrow{B}}} = \sum_{k=0}^{\infty} \frac{\overrightarrow{\overrightarrow{B}}^k}{k!} = \begin{pmatrix} \sum_{k=0}^{\infty} a^k (t-t_0)^k/k! & 0 \\ 0 & \sum_{k=0}^{\infty} b^k (t-t_0)^k/k! \end{pmatrix} = \begin{pmatrix} e^{a(t-t_0)} & 0 \\ 0 & e^{b(t-t_0)} \end{pmatrix}. \tag{C.5}$$

So in the case of a diagonal matrix, the exponent of a matrix is the matrix of the exponents of its elements. In general, this is not the case. Assume now the matrix $\overrightarrow{\overrightarrow{B}}$ is diagonalizable, *i.e.* $\det \overrightarrow{\overrightarrow{B}} = (ab - |c|^2)(t-t_0)^2 \neq 0$. The eigenvalues $\lambda_{1,2}$ can be calculated, as follows:

$$\lambda_{1,2} = \frac{\mathrm{Tr}(\overrightarrow{\overrightarrow{B}})}{2} \pm \frac{\sqrt{\det(\overrightarrow{\overrightarrow{B}})^2 - 4\mathrm{Tr}(\overrightarrow{\overrightarrow{B}})}}{2} \quad \text{where} \quad \det(\overrightarrow{\overrightarrow{B}}) = (ab - |c|^2)(t-t_0)^2 \quad \text{and} \quad \mathrm{Tr}(\overrightarrow{\overrightarrow{B}}) = (a+b)(t-t_0). \tag{C.6}$$

Using the relation $\overrightarrow{\overrightarrow{B}} \vec{u}_{1,2} = \lambda_{1,2} \vec{u}_{1,2}$ and by using the fact that the matrix $\overrightarrow{\overrightarrow{B}}$ is Hermitian and non-diagonal, the eigenvectors can be calculated by

$$\vec{u}_{1,2} = \frac{1}{\sqrt{1 + |\alpha_{1,2}|^2}} \begin{pmatrix} 1 \\ \alpha_{1,2} \end{pmatrix} \qquad \text{where} \qquad \alpha_{1,2} = \frac{a - \lambda_{1,2}}{c^*} \tag{C.7}$$

Using the eigenvectors, the matrix $\overrightarrow{\overrightarrow{B}}$ is diagonalized by the matrix U containing the eigenvectors:

$$\overrightarrow{\overrightarrow{U}} = \begin{pmatrix} \vec{u}_1 & \vec{u}_2 \end{pmatrix} = \begin{pmatrix} u_{11} & u_{21} \\ u_{12} & u_{22} \end{pmatrix} \qquad \text{such that} \qquad \overrightarrow{\overrightarrow{B}} = \overrightarrow{\overrightarrow{U}} \begin{pmatrix} \lambda_1 & 0 \\ 0 & \lambda_2 \end{pmatrix} \overrightarrow{\overrightarrow{U}}^{\dagger}. \tag{C.8}$$

The matrix U has another nice property. Its Hermitian conjugate being its inverse $\overrightarrow{\overrightarrow{U}}^{\dagger} = \overrightarrow{\overrightarrow{U}}^{-1}$. Calculating powers of $\overrightarrow{\overrightarrow{A}}$ can now easily be done, yielding

$$\overrightarrow{\overrightarrow{B}}^k = \underbrace{\overrightarrow{\overrightarrow{U}} \begin{pmatrix} \lambda_1 & 0 \\ 0 & \lambda_2 \end{pmatrix} \overrightarrow{\overrightarrow{U}}^{\dagger} \cdots \overrightarrow{\overrightarrow{U}} \begin{pmatrix} \lambda_1 & 0 \\ 0 & \lambda_2 \end{pmatrix} \overrightarrow{\overrightarrow{U}}^{\dagger}}_{k \text{ times}} = \overrightarrow{\overrightarrow{U}} \begin{pmatrix} \lambda_1^k & 0 \\ 0 & \lambda_2^k \end{pmatrix} \overrightarrow{\overrightarrow{U}}^{\dagger}, \tag{C.9}$$

where the property that $\overrightarrow{\overrightarrow{U}}^{\dagger}\overrightarrow{\overrightarrow{U}} = \mathbf{1}_2$ is extensively used. Using the property of Eq. (C.9), it is easy to calculate the exponent of matrix $\overrightarrow{\overrightarrow{B}}$. The result is

$$e^{\overrightarrow{\overrightarrow{A}}(t-t_0)} = \sum_{k=0}^{\infty} \frac{\overrightarrow{\overrightarrow{A}}^k}{k!}(t-t_0)^k = \overrightarrow{\overrightarrow{U}} \left[\sum_{k=0}^{\infty} \frac{1}{k!} \begin{pmatrix} \lambda_1^k & 0 \\ 0 & \lambda_2^k \end{pmatrix} \right] \overrightarrow{\overrightarrow{U}}^{\dagger} = \overrightarrow{\overrightarrow{U}} \begin{pmatrix} e^{\lambda_1} & 0 \\ 0 & e^{\lambda_2} \end{pmatrix} \overrightarrow{\overrightarrow{U}}^{\dagger}. \tag{C.10}$$

The solution to Eq. (C.1) is given by

$$\vec{v}(t) = e^{\overrightarrow{\overrightarrow{A}}(t-t_0)} \vec{v}(t_0). \tag{C.11}$$

This result is used to perform the time steps in the simulation.

References

[1] J. F. Allen and A. D. Misener. Flow Phenomena in Liquid Helium II. *Nature*, 142:643–644, October 1938.

[2] P. Kapitza. Viscosity of Liquid Helium below the λ-Point. *Nature*, 141:74, January 1938.

[3] M. H. Anderson, J. R. Ensher, M. R. Matthews, C. E. Wieman, and E. A. Cornell. Observation of bose-einstein condensation in a dilute atomic vapor. *Science*, 269(5221):198–201, 1995.

[4] J. R. Abo-Shaeer, C. Raman, J. M. Vogels, and W. Ketterle. Observation of vortex lattices in bose-einstein condensates. *Science*, 292(5516):476–479, 2001.

[5] Michael P. Bradley, James V. Porto, Simon Rainville, James K. Thompson, and David E. Pritchard. Penning trap measurements of the masses of ^{133}Cs, ^{87,85}Rb, and ^{23}Na with uncertainties ≤ 0.2 ppb. *Phys. Rev. Lett.*, 83:4510–4513, Nov 1999.

[6] Robert C. Weast. *Handdbook of Chemistry and Physics, 49th Edition*. CRC, 1968.

[7] C. Samuelis, E. Tiesinga, T. Laue, M. Elbs, H. Knöckel, and E. Tiemann. Cold atomic collisions studied by molecular spectroscopy. *Phys. Rev. A*, 63:012710, Dec 2000.

[8] D. Steck. Sodium D-line data.

[9] Charly Beulenkamp. Evaporative cooling in a Bose gas, September 2015.

[10] C. Pethick and H. Smith. *Bose-Einstein condensation in dilute gases*. Cambridge University Press, 2002.

[11] P. van der Straten and H. Metcalf. *Atoms and Molecules interacting with light*. Cambridge University Press, 2016.

[12] LCoS-SLM X10468 series OPERATION MANUAL.

[13] L. Salasnich, A. Parola, and L. Reatto. Effective wave equations for the dynamics of cigar-shaped and disk-shaped bose condensates. *Phys. Rev. A*, 65:043614, Apr 2002.

[14] S. Inouye, A. P. Chikkatur, D. M. Stamper-Kurn, J. Stenger, D. E. Pritchard, and W. Ketterle. Superradiant rayleigh scattering from a bose-einstein condensate. *Science*, 285:571–574, July 1999.